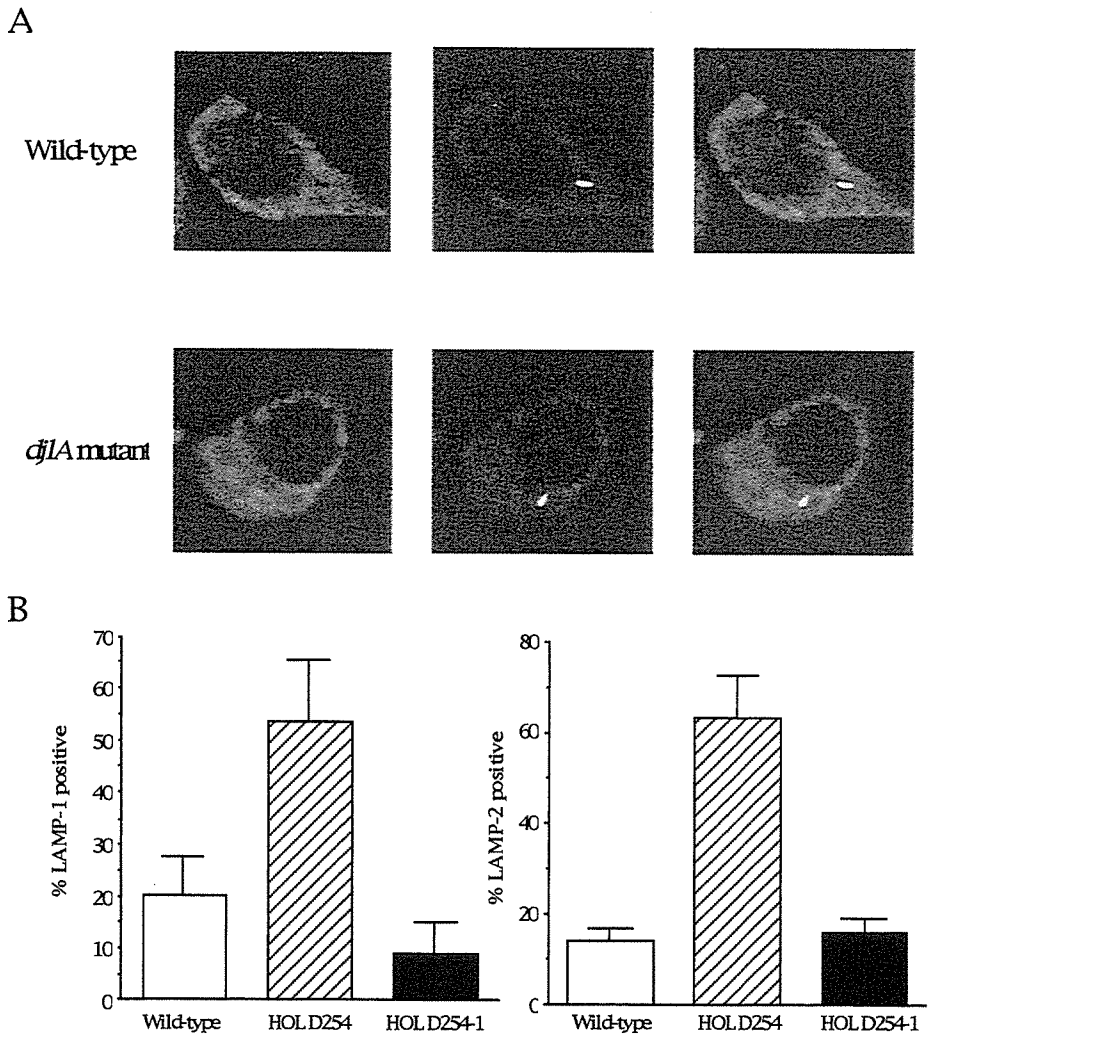

FIG. 4. Colocalization of the intracellular growth mutant with late endosomal/lysosomal marker LAMP-1 or LAMP-2 in J774 mouse macrophage cells by confocal laser-scanning microscopy. J774 macrophages were incubated with the *L. dumoffii* mutant or wild-type strain for 4 h. (A) Late endosomes and lysosomes stained with rat monoclonal antibody 1D4B, specific for LAMP-1, and Cy3-labeled anti-rat secondary antibody (red) are shown on the left. Bacteria stained with rabbit polyclonal antibody specific for *L. dumoffii* Tex-KL and Alexa488-labeled anti-rabbit secondary antibody (green) are shown in the middle. Merged images showing LAMP-1-positive bacteria (yellow) and LAMP-1-negative bacteria (green) are shown on the right. (B) Data were collected from about 100 intracellular bacteria in total. The percentage that is LAMP-1 or LAMP-2 positive was calculated by dividing the number of colocalizing intracellular bacteria by the total number of intracellular bacteria scored. The average and standard deviation described here were calculated from three coverslips per strain in two independent experiments.

undertaken to understand the intracellular life cycle of *L. pneumophila*, very few species other than *L. pneumophila* have been examined phenotypically. The aim of this study was to uncover how *L. dumoffii* survives and replicates in mammalian cells and to identify the genes of *L. dumoffii* needed for intracellular growth. We isolated 4 mutants that were defective in intracellular growth in macrophages and alveolar epithelial cells among 790 independently derived Tn*903*dII*lacZ* mutants of *L. dumoffii*. The defect in intracellular growth of these four mutants cannot be attributed to a defect in adherence or entry, because almost equal numbers of mutants and wild-type cells were present within mammalian cells at 0 h postinfection. Two of the four mutants had a transposon insertion in either the *dotC* or *icmB* homologues (5, 51, 60). The *dot/icm* genes are required for intracellular multiplication of *L. pneumophila* (5, 51, 60). Our results suggest that the *dotC* and *icmB* genes of *L. dumoffii* and *L. pneumophila* appear to perform similar functions. We propose that the *dot/icm* genes are involved in the pathogenesis of most *Legionella* species, since these genes are important in the intracellular growth of these distinct *Legionella* species.

One of the mutants defective in intracellular growth was shown to have a transposon insertion in the gene which had sequence similarity to the *djlA* gene (16). Cloning and sequence analysis of this gene revealed that the primary structure of *L. dumoffii* DjlA showed homology to other bacterial DjlA proteins (10, 16, 73). DjlA is the third DnaK cochaperone of *E. coli*, containing a J domain highly conserved in the DnaJ/

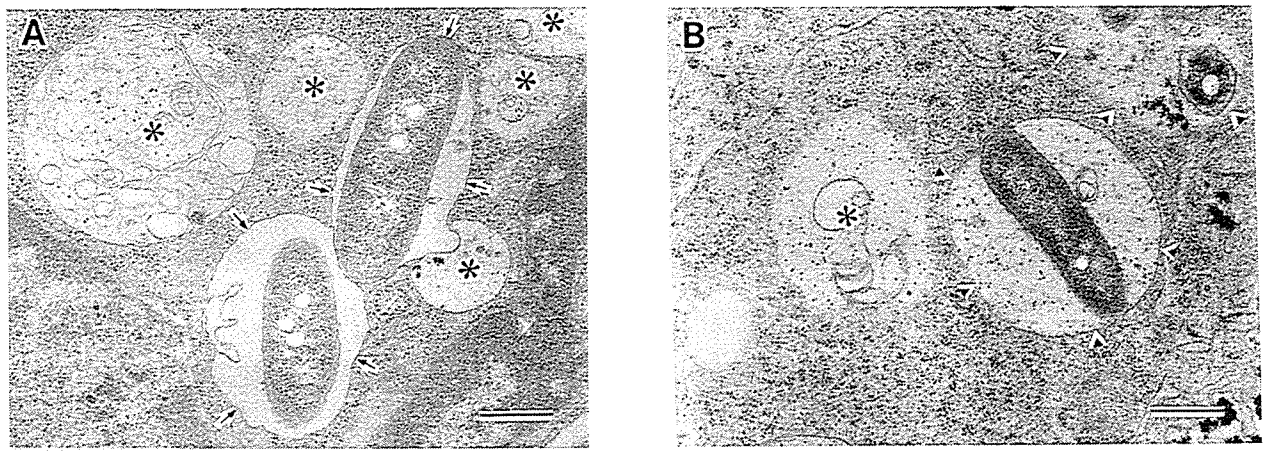

FIG. 5. Distribution of a lysosomal marker, BSA-gold, in phagosomes containing the wild-type strain or the *djlA* mutant strain. To label the lysosomal compartment, J774 cells were incubated with 15-nm BSA-gold overnight, washed, and then chased for 3 h. Cells were then infected with wild-type strain (A) or *djlA* mutant strain (B). At 4 h postinfection, the cells were fixed and processed for electron microscopy. Arrows in panel A indicate phagosomes containing no detectable gold; arrowheads in panel B indicate phagolysosomes containing BSA-gold; asterisks indicate, lysosomes containing BSA-gold. Bar, 0.5 μm.

Hsp40 family of molecular chaperones, including DnaJ and CbpA (16, 27, 65). CbpA is 39% identical to DnaJ along its entire length (64), while DjlA does not have any sequence similarity other than the J domain to DnaJ and CbpA in *E. coli* (26, 37). DjlA is unique in its structure and location in the DnaJ family. The J domain resides in the C terminus of DjlA but in the N terminus of other DnaJ family proteins. The N terminus of DjlA is integrated into the inner membrane through the single TMD, and the C-terminal J domain is located in the cytoplasm (16), while the whole of DnaJ and CbpA is localized in the cytoplasm. Moderate overproduction of *djlA* can trigger the synthesis of the colanic acid capsule in *E. coli*, mediated by the two-component regulatory system RcsC-RcsB, cooperating with DnaK and GrpE, but not DnaJ (15, 27, 37, 73). Unlike CbpA, DjlA could not adequately complement bacteriophage λ growth in a DnaJ-null background or restore bacterial growth above 40°C or below 16°C in the *dnaJ cbpA* null background in *E. coli* (15, 26, 37). The DjlA deletion mutant exhibits no apparent growth phenotype in *E. coli* (15, 16, 26). Thus, the true role of DjlA has been unclear.

We demonstrated that the *djlA* mutant of *L. dumoffii* exhibited a defective growth phenotype in mammalian cells and protozoan hosts. Phagosomes containing wild-type *L. dumoffii* excluded the late endosomal/lysosomal markers LAMP-1 and LAMP-2 and a lysosomal marker, BSA-gold, and were surrounded by RER in J774 macrophages, while *djlA* mutant-bearing phagosomes contained LAMP-1, LAMP-2, and BSA-gold and were not surrounded by RER (Fig. 4 to 6). It has been

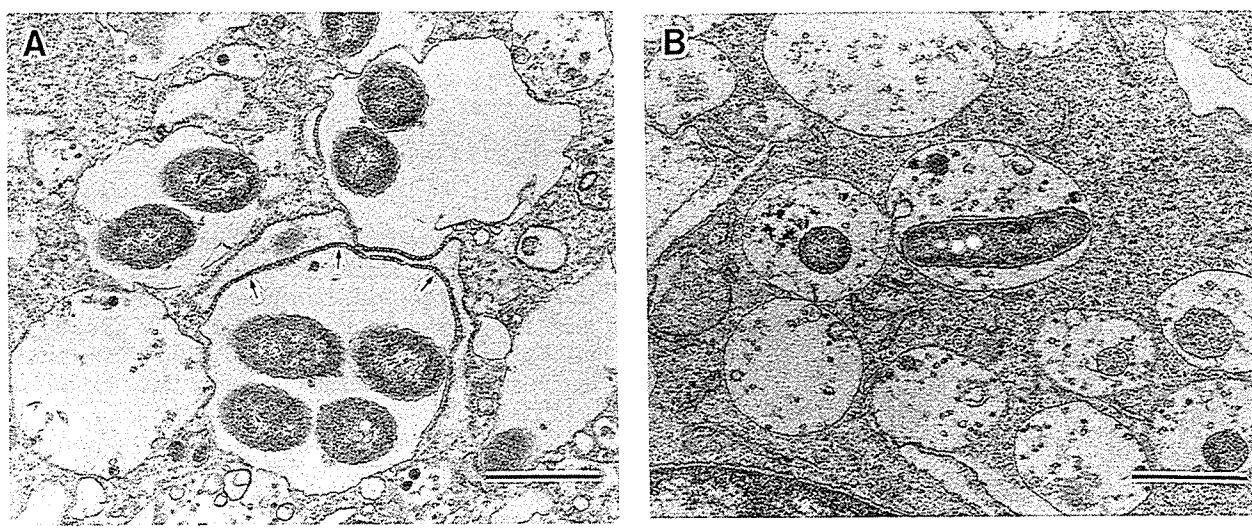

FIG. 6. Transmission electron micrographs of J774 mouse macrophages infected by the wild-type *L. dumoffii* (A) and the *djlA* mutant HOLD254 (B) at 8 h after infection. (A) Wild-type *L. dumoffii*-containing phagosomes were surrounded by RER (arrows). (B) HOLD254-containing phagosomes appeared to harbor much debris resulting from fusing lysosomes. Bar, 1.0 μm.

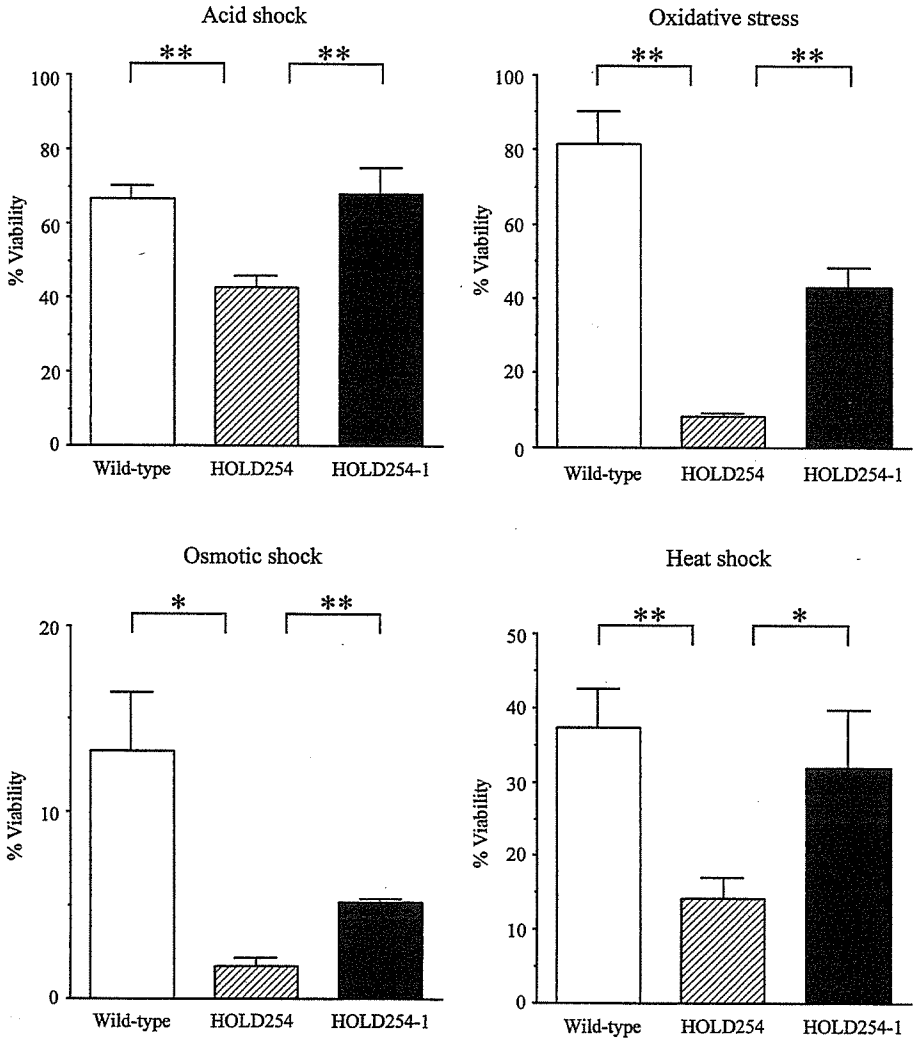

FIG. 7. Sensitivities of in vitro-grown stationary-phase wild-type *L. dumoffii* (open bars), the *djlA* mutant strain (hatched bars), and the *djlA* complemented strain (solid bars) to oxidative stress, osmotic stress, acid stress, and heat shock (10 mM hydrogen peroxide for 30 min, 5 M sodium chloride for 30 min, pH 3 for 5 min, and 48°C for 60 min, respectively). Stationary-phase cultures were exposed to each stress as described in Materials and Methods. The percentage of viable bacteria was calculated by dividing the CFU obtained from plating the bacteria onto BCYE agar plates following exposure to the indicated stress by the CFU of the bacteria obtained from plating the bacteria onto BCYE agar plates prior to exposure to the stress and multiplying by 100. Experiments were performed at least three times, and the results represent the mean and standard deviation. Results were analyzed for significance by analysis of variance and by a two-tailed, unpaired *t* test. Asterisks indicate significant differences between the *djlA* mutant and two other strains. (*, $P < 0.01$; **, $P < 0.001$).

reported that *L. pneumophila* is targeted into RER-surrounding phagosomes that do not fuse with lysosomes in mammalian cells (25, 33), while *L. micdadei* is targeted into RER-free phagosomes that are thought to fuse to lysosomes in mammalian cells (3, 36). Doyle et al. (20) reported that virulent *L. longbeachae*-containing phagosomes were surrounded by RER but avirulent *L. longbeachae*-containing phagosomes did not have RER. Our observations suggest that *L. dumoffii* might replicate in phagosomes which have not fused with lysosomes and are able to recruit host cell organelles, similar to that reported for *L. pneumophila*. The *djlA* mutant seemed to be intact (Fig. 5B), and no loss of CFU was observed during the infection (Fig. 1A and 2A). It is possible that the mutant bacteria are in either a late endosomal or a nondegradative lysosomal compartment, as described by Joshi et al. (35). The frequency of recruitment of *L. dumoffii* RER at 8 h is lower than that reported for *L. pneumophila* (32). We suspect that association with ER and avoidance of lysosomes by *L. dumoffii* is temporary, as shown for *L. pneumophila* (63).

Although the precise function of DjlA is unclear, it does not seem to play a direct role in intracellular trafficking. DjlA might contribute to folding or transportation of the proteins, such as Dot/Icm proteins, which play an important role in intracellular survival and growth. Most of the Dot/Icm proteins are located in the bacterial membranes, where they may associate to form a large transport complex, the type IV secretion apparatus (17, 43, 51, 60, 61). DjlA might cooperate with Dot/Icm proteins through their interaction in the membranes, since the N-terminal portion of DjlA is located in the cytoplastic membrane (16, 37). It has been reported that the two-

component regulatory system, PhoP-PhoQ, of *Salmonella enterica* serovar Typhimurium plays an essential role in survival within macrophages (28). It is possible that DjlA promotes *L. dumoffii* to adapt to intracellular environments and to coordinate with the two-component signal transduction systems. In vitro, DjlA-deficient mutants showed an increased susceptibility to several stresses, including oxidative stress, that might be encountered by bacteria in mammalian cells. DjlA might protect the genes or proteins, including Dot/Icm and catalase-peroxidase (7), that are important for intracellular growth, from harmful stress in a direct or indirect manner. Several lines of evidence for the important role of stress proteins in intracellular growth and virulence have been reported for intracellular pathogens; these include DnaK of *Brucella suis* (38), ClpC and ClpP of *Listeria monocytogenes* (24, 54), Lon of *B. abortus* (53), and GsrA of *Yersinia enterocolitica* (69). In *L. pneumophila*, at least 30 proteins are included during the intracellular infection of macrophages and at least 13 of these proteins, including GroEL (Hsp60), GroES, and GspA, are also induced by several stress conditions in vitro (1, 2, 21). Recently, Pedersen et al. (50) demonstrated direct evidence for the role of the stress protein of *L. pneumophila*, HtrA, during intracellular growth in mammalian cells but not in protozoan cells. Our data indicated that DjlA plays an important role during intracellular growth in both mammalian and protozoan cells. Besides Dot/Icm proteins, stress proteins or molecular chaperones might play an important role in the intracellular growth of the *Legionella* species.

In conclusion, we showed the essential role of *L. dumoffii* Dot/Icm homologues and DjlA during the intracellular infection of mammalian cells and protozoa. The precise mechanism of DjlA involvement in intracellular multiplication, including interaction with DnaK, remains to be elucidated. Further investigation of specific substrates with which DjlA interacts will lead to a better understanding of the intracellular survival mechanism in the *Legionella* species.

ACKNOWLEDGMENTS

We acknowledge H. A. Shuman for his generous gifts of plasmids pLAW330 and the pMMB207c. We thank H. Nakayama and C. C. Sze for scientific discussion. We also thank H. Fujita, K. Iida, and H. Kajiwara for technical assistance. We thank L. Saza for manuscript preparation.

This work was supported by grants-in-aid for scientific research (B)(2)14370094, (B)(1)12490009, and (C)(2)15590391 from the Ministry of Education, Science, Culture and Sports of Japan. This work was also supported by Health and Labour Sciences research grants (H15-Ganyobou-095) from the Ministry of Health, Labour and Welfare.

REFERENCES

1. **Abu Kwaik, Y., B. I. Eisenstein, and N. C. Engleberg.** 1993. Phenotypic modulation by *Legionella pneumophila* upon infection of macrophages. Infect. Immun. **61:**1320–1329.
2. **Abu Kwaik, Y., L. Y. Gao, O. S. Harb, and B. J. Stone.** 1997. Transcriptional regulation of the macrophage-induced gene (*gspA*) of *Legionella pneumophila* and phenotypic characterization of a null mutant. Mol. Microbiol. **24:**629–642.
3. **Abu Kwaik, Y., C. Venkataraman, O. S. Harb, and L. Y. Gao.** 1998. Signal transduction in the protozoan host *Hartmannella vermiformis* upon attachment and invasion by *Legionella micdadei*. Appl. Environ. Microbiol. **64:** 3134–3139.
4. **Alli, O. A., S. Zink, N. K. Von Lackum, and Y. Abu-Kwaik.** 2003. Comparative assessment of virulence traits in *Legionella* spp. Microbiology **149:**631–641.
5. **Andrews, H. L., J. P. Vogel, and R. R. Isberg.** 1998. Identification of linked *Legionella pneumophila* genes essential for intracellular growth and evasion of the endocytic pathway. Infect. Immun. **66:**950–958.
6. **Baine, W. B.** 1985. Cytolytic and phospholipase C activity in *Legionella* species. J. Gen. Microbiol. **131:**1383–1391.
7. **Bandyopadhyay, P., B. Byrne, Y. Chan, M. S. Swanson, and H. M. Steinman.** 2003. *Legionella pneumophila* catalase-peroxidases are required for proper trafficking and growth in primary macrophages. Infect. Immun. **71:**4526–4535.
8. **Benin, A. L., R. F. Benson, and R. E. Besser.** 2002. Trends in legionnaires disease, 1980–1998: declining mortality and new patterns of diagnosis. Clin. Infect. Dis. **35:**1039–1046.
9. **Bozue, J. A., and W. Johnson.** 1996. Interaction of *Legionella pneumophila* with *Acanthamoeba castellanii*: uptake by coiling phagocytosis and inhibition of phagosome-lysosome fusion. Infect. Immun. **64:**668–673.
10. **Brabetz, W., C. E. Schirmer, and H. Brade.** 2000. 3-Deoxy-D-*manno*-oct-2-ulosonic acid (Kdo) transferase of *Legionella pneumophila* transfers two Kdo residues to a structurally different lipid A precursor of *Escherichia coli*. J. Bacteriol. **182:**4654–4657.
11. **Brenner, D. J.** 1985. The new species of *Legionella*. Int. J. Syst. Bacteriol. **35:**50–59.
12. **Byrne, B., and M. S. Swanson.** 1998. Expression of *Legionella pneumophila* virulence traits in response to growth conditions. Infect. Immun. **66:**3029–3034.
13. **Casaregola, S., M. Chen, N. Bouquin, V. Norris, A. Jacq, M. Goldberg, S. Margarson, M. Tempete, S. McKenna, H. Sweetman, et al.** 1991. Analysis of a myosin-like protein and the role of calcium in the *E. coli* cell cycle. Res. Microbiol. **142:**201–207.
14. **Chen, L., Y. Chen, D. W. Wood, and E. W. Nester.** 2002. A new type IV secretion system promotes conjugal transfer in *Agrobacterium tumefaciens*. J. Bacteriol. **184:**4838–4845.
15. **Clarke, D. J., L. B. Holland, and A. Jacq.** 1997. Point mutations in the transmembrane domain of DjlA, a membrane-linked DnaJ-like protein, abolish its function in promoting colanic acid production via the Res signal transduction pathway. Mol. Microbiol. **25:**933–944.
16. **Clarke, D. J., A. Jacq, and I. B. Holland.** 1996. A novel DnaJ-like protein in *Escherichia coli* inserts into the cytoplasmic membrane with a type III topology. Mol. Microbiol. **20:**1273–1286.
17. **Coers, J., J. C. Kagan, M. Matthews, H. Nagai, D. M. Zuckman, and C. R. Roy.** 2000. Identification of Icm protein complexes that play distinct roles in the biogenesis of an organelle permissive for *Legionella pneumophila* intracellular growth. Mol. Microbiol. **38:**719–736.
18. **Cordes, L. G., H. W. Wilkinson, G. W. Gorman, B. J. Fikes, and D. W. Fraser.** 1979. Atypical *Legionella*-like organisms: fastidious water-associated bacteria pathogenic for man. Lancet **ii:**927–930.
19. **Da Silva, T. R., J. R. De Freitas, Q. C. Silva, C. P. Figueira, E. Roxo, S. C. Leao, I. A. De Freitas, and P. S. Veras.** 2002. Virulent *Mycobacterium fortuitum* restricts NO production by a gamma interferon-activated J774 cell line and phagosome-lysosome fusion. Infect. Immun. **70:**5628–5634.
20. **Doyle, R. M., N. P. Cianciotto, S. Banvi, P. A. Manning, and M. W. Heuzenroeder.** 2001. Comparison of virulence of *Legionella longbeachae* strains in guinea pigs and U937 macrophage-like cells. Infect. Immun. **69:**5335–5344.
21. **Fernandez, R. C., S. M. Logan, S. H. Lee, and P. S. Hoffman.** 1996. Elevated levels of *Legionella pneumophila* stress protein Hsp60 early in infection of human monocytes and L929 cells correlate with virulence. Infect. Immun. **64:**1968–1976.
22. **Fields, B. S.** 1996. The molecular ecology of legionellae. Trends Microbiol. **4:**286–290.
23. **Furuno, K., T. Ishikawa, K. Akasaki, S. Yano, Y. Tanaka, Y. Yamaguchi, H. Tsuji, M. Himeno, and K. Kato.** 1989. Morphological localization of a major lysosomal membrane glycoprotein in the endocytic membrane system. J. Biochem. (Tokyo) **106:**708–716.
24. **Gaillot, O., E. Pellegrini, S. Bregenholt, S. Nair, and P. Berche.** 2000. The ClpP serine protease is essential for the intracellular parasitism and virulence of *Listeria monocytogenes*. Mol. Microbiol. **35:**1286–1294.
25. **Gao, L. Y., O. S. Harb, and Y. A. Kwaik.** 1998. Identification of macrophage-specific infectivity loci (*mil*) of *Legionella pneumophila* that are not required for infectivity of protozoa. Infect. Immun. **66:**883–892.
26. **Genevaux, P., F. Schwager, C. Georgopoulos, and W. L. Kelley.** 2001. The *djlA* gene acts synergistically with *dnaJ* in promoting *Escherichia coli* growth. J. Bacteriol. **183:**5747–5750.
27. **Genevaux, P., A. Wawrzynow, M. Zylicz, C. Georgopoulos, and W. L. Kelley.** 2001. DjlA is a third DnaK co-chaperone of *Escherichia coli*, and DjlA-mediated induction of colanic acid capsule requires DjlA-DnaK interaction. J. Biol.Chem. **276:**7906–7912.
28. **Groisman, E. A.** 2001. The pleiotropic two-component regulatory system PhoP-PhoQ. J. Bacteriol. **183:**1835–1842.
29. **Hales, L. M., and H. A. Shuman.** 1999. The *Legionella pneumophila rpoS* gene is required for growth within *Acanthamoeba castellanii*. J. Bacteriol. **181:**4879–4889.
30. **Hanahan, D.** 1983. Studies on transformation of *Escherichia coli* with plasmids. J. Mol. Biol. **166:**557–580.
31. **Hohn, B., and J. Collins.** 1980. A small cosmid for efficient cloning of large DNA fragments. Gene **11:**291–298.

32. **Horwitz, M. A.** 1983. Formation of a novel phagosome by the Legionnaires' disease bacterium (*Legionella pneumophila*) in human monocytes. J. Exp. Med. **158**:1319–1331.
33. **Horwitz, M. A.** 1983. The Legionnaires' disease bacterium (*Legionella pneumophila*) inhibits phagosome-lysosome fusion in human monocytes. J. Exp. Med. **158**:2108–2126.
34. **Horwitz, M. A., and F. R. Maxfield.** 1984. *Legionella pneumophila* inhibits acidification of its phagosome in human monocytes. J. Cell Biol. **99**:1936–1943.
35. **Joshi, A. D., S. Sturgill-Koszycki, and M. S. Swanson.** 2001. Evidence that Dot-dependent and -independent factors isolate the *Legionella pneumophila* phagosome from the endocytic network in mouse macrophages. Cell. Microbiol. **3**:99–114.
36. **Joshi, A. D., and M. S. Swanson.** 1999. Comparative analysis of *Legionella pneumophila* and *Legionella micdadei* virulence traits. Infect. Immun. **67**: 4134–4142.
37. **Kelley, W. L., and C. Georgopoulos.** 1997. Positive control of the two-component RcsC/B signal transduction network by DjlA: a member of the DnaJ family of molecular chaperones in *Escherichia coli*. Mol. Microbiol. **25**:913–931.
38. **Kohler, S., J. Teyssier, A. Cloeckaert, B. Rouot, and J. P. Liautard.** 1996. Participation of the molecular chaperone DnaK in intracellular growth of *Brucella suis* within U937-derived phagocytes. Mol. Microbiol. **20**:701–712.
39. **Kuronita, T., E. L. Eskelinen, H. Fujita, P. Saftig, M. Himeno, and Y. Tanaka.** 2002. A role for the lysosomal membrane protein LGP85 in the biogenesis and maintenance of endosomal and lysosomal morphology. J. Cell Sci. **115**:4117–4131.
40. **Lewallen, K. R., R. M. McKinney, D. J. Brenner, C. W. Moss, D. H. Dail, B. M. Thomason, and R. A. Bright.** 1979. A newly identified bacterium phenotypically resembling, but genetically distinct from, *Legionella pneumophila*: an isolate in a case of pneumonia. Ann. Intern. Med. **91**:831–834.
41. **Maruta, K., H. Miyamoto, T. Hamada, M. Ogawa, H. Taniguchi, and S. Yoshida.** 1998. Entry and intracellular growth of *Legionella dumoffii* in alveolar epithelial cells. Am. J. Respir. Crit. Care Med. **157**:1967–1974.
42. **Maruta, K., M. Ogawa, H. Miyamoto, K. Izu, and S. I. Yoshida.** 1998. Entry and intracellular localization of *Legionella dumoffii* in Vero cells. Microb. Pathog. **24**:65–73.
43. **Matthews, M., and C. R. Roy.** 2000. Identification and subcellular localization of the *Legionella pneumophila* IcmX protein: a factor essential for establishment of a replicative organelle in eukaryotic host cells. Infect. Immun. **68**:3971–3982.
44. **Miyamoto, H., H. Taniguchi, and S. Yoshida.** 2003. A simple qualitative assay for intracellular growth of *Legionella pneumophila* within *Acanthamoeba culbertsoni*. Kansenshogaku Zasshi. **77**:343–345. (In Japanese)
45. **Miyamoto, H., S. I. Yoshida, H. Taniguchi, and H. A. Shuman.** 2003. Virulence conversion of *Legionella pneumophila* by conjugal transfer of chromosomal DNA. J. Bacteriol. **185**:6712–6718.
46. **Moffat, J. F., and L. S. Tompkins.** 1992. A quantitative model of intracellular growth of *Legionella pneumophila* in *Acanthamoeba castellanii*. Infect. Immun. **60**:296–301.
47. **Morales, V. M., A. Backman, and M. Bagdasarian.** 1991. A series of wide-host-range low-copy-number vectors that allow direct screening for recombinants. Gene **97**:39–47.
48. **Nagai, H., and C. R. Roy.** 2001. The DotA protein from *Legionella pneumophila* is secreted by a novel process that requires the Dot/Icm transporter. EMBO J. **20**:5962–5970.
49. **Padmalayam, I., K. Karem, B. Baumstark, and R. Massung.** 2000. The gene encoding the 17-kDa antigen of *Bartonella henselae* is located within a cluster of genes homologous to the *virB* virulence operon. DNA Cell Biol. **19**:377–382.
50. **Pedersen, L. L., M. Radulic, M. Doric, and Y. Abu Kwaik.** 2001. HtrA homologue of *Legionella pneumophila*: an indispensable element for intracellular infection of mammalian but not protozoan cells. Infect. Immun. **69**:2569–2579.
51. **Purcell, M., and H. A. Shuman.** 1998. The *Legionella pneumophila icmGCDJBF* genes are required for killing of human macrophages. Infect. Immun. **66**:2245–2255.
52. **Quinn, F. D., M. G. Keen, and L. S. Tompkins.** 1989. Genetic, immunological, and cytotoxic comparisons of *Legionella* proteolytic activities. Infect. Immun. **57**:2719–2725.
53. **Robertson, G. T., M. E. Kovach, C. A. Allen, T. A. Ficht, and R. M. Roop, Jr.** 2000. The *Brucella abortus* Lon functions as a generalized stress response protease and is required for wild-type virulence in BALB/c mice. Mol. Microbiol. **35**:577–588.
54. **Rouquette, C., C. de Chastellier, S. Nair, and P. Berche.** 1998. The ClpC ATPase of *Listeria monocytogenes* is a general stress protein required for virulence and promoting early bacterial escape from the phagosome of macrophages. Mol. Microbiol. **27**:1235–1245.
55. **Roy, C. R., K. H. Berger, and R. R. Isberg.** 1998. *Legionella pneumophila* DotA protein is required for early phagosome trafficking decisions that occur within minutes of bacterial uptake. Mol. Microbiol. **28**:663–674.
56. **Roy, C. R., and L. G. Tilney.** 2002. The road less traveled: transport of *Legionella* to the endoplasmic reticulum. J. Cell Biol. **158**:415–419.
57. **Sadosky, A. B., L. A. Wiater, and H. A. Shuman.** 1993. Identification of *Legionella pneumophila* genes required for growth within and killing of human macrophages. Infect. Immun. **61**:5361–5373.
58. **Sambrook, J., and W. J. Russell.** 2001. Molecular cloning: a laboratory manual, 3rd ed. Cold Spring Harbor Laboratory Press, Cold Spring Harbor, N.Y.
59. **Schulein, R., and C. Dehio.** 2002. The VirB/VirD4 type IV secretion system of *Bartonella* is essential for establishing intraerythrocytic infection. Mol. Microbiol. **46**:1053–1067.
60. **Segal, G., M. Purcell, and H. A. Shuman.** 1998. Host cell killing and bacterial conjugation require overlapping sets of genes within a 22-kb region of the *Legionella pneumophila* genome. Proc. Natl. Acad. Sci. USA **95**:1669–1674.
61. **Segal, G., and H. A. Shuman.** 1998. How is the intracellular fate of the *Legionella pneumophila* phagosome determined? Trends Microbiol. **6**:253–255.
62. **Small, P. L., L. Ramakrishnan, and S. Falkow.** 1994. Remodeling schemes of intracellular pathogens. Science **263**:637–639.
63. **Sturgill-Koszycki, S., and M. S. Swanson.** 2000. *Legionella pneumophila* replication vacuoles mature into acidic, endocytic organelles. J. Exp. Med. **192**:1261–1272.
64. **Ueguchi, C., M. Kakeda, H. Yamada, and T. Mizuno.** 1994. An analogue of the DnaJ molecular chaperone in *Escherichia coli*. Proc. Natl. Acad. Sci. USA **91**:1054–1058.
65. **Ueguchi, C., T. Shiozawa, M. Kakeda, H. Yamada, and T. Mizuno.** 1995. A study of the double mutation of *dnaJ* and *cbpA*, whose gene products function as molecular chaperones in *Escherichia coli*. J. Bacteriol. **177**:3894–3896.
66. **Wai, S. N., Y. Mizunoe, A. Takade, S. I. Kawabata, and S. I. Yoshida.** 1998. *Vibrio cholerae* O1 strain TSI-4 produces the exopolysaccharide materials that determine colony morphology, stress resistance, and biofilm formation. Appl. Environ. Microbiol. **64**:3648–3655.
67. **Wall, D., M. Zylicz, and C. Georgopoulos.** 1994. The NH_2-terminal 108 amino acids of the *Escherichia coli* DnaJ protein stimulate the ATPase activity of DnaK and are sufficient for lambda replication. J. Biol. Chem. **269**:5446–5451.
68. **Wiater, L. A., A. B. Sadosky, and H. A. Shuman.** 1994. Mutagenesis of *Legionella pneumophila* using Tn*903* dI*lacZ*: identification of a growth-phase-regulated pigmentation gene. Mol. Microbiol. **11**:641–653.
69. **Yamamoto, T., T. Hanawa, S. Ogata, and S. Kamiya.** 1996. Identification and characterization of the *Yersinia enterocolitica gsrA* gene, which protectively responds to intracellular stress induced by macrophage phagocytosis and to extracellular environmental stress. Infect. Immun. **64**:2980–2987.
70. **Yanisch-Perron, C., J. Vieira, and J. Messing.** 1985. Improved M13 phage cloning vectors and host strains: nucleotide sequences of the M13mp 18 and pUC19 vectors. Gene **33**:103–119.
71. **Yu, V. L., J. F. Plouffe, M. C. Pastoris, J. E. Stout, M. Schousboe, A. Widmer, J. Summersgill, T. File, C. M. Heath, D. L. Paterson, and A. Chereshsky.** 2002. Distribution of *Legionella* species and serogroups isolated by culture in patients with sporadic community-acquired legionellosis: an international collaborative survey. J. Infect. Dis. **186**:127–128.
72. **Yura, T., H. Mori, H. Nagai, T. Nagata, A. Ishihama, N. Fujita, K. Isono, K. Mizobuchi, and A. Nakata.** 1992. Systematic sequencing of the *Escherichia coli* genome: analysis of the 0–2.4 min region. Nucleic Acids Res. **20**:3305–3308.
73. **Zuber, M., T. A. Hoover, and D. L. Court.** 1995. Analysis of a *Coxiella burnetti* gene product that activates capsule synthesis in *Escherichia coli*: requirement for the heat shock chaperone DnaK and the two-component regulator RcsC. J. Bacteriol. **177**:4238–4244.
74. **Zuckman, D. M., J. B. Hung, and C. R. Roy.** 1999. Pore-forming activity is not sufficient for *Legionella pneumophila* phagosome trafficking and intracellular growth. Mol. Microbiol. **32**:990–1001.

Editor: S. H. E. Kaufmann

Confocal imaging of biofilm formation process using fluoroprobed *Escherichia coli* and fluoro-stained exopolysaccharide

Ryo Maeyama,[1,2] Yoshimitsu Mizunoe,[3] James M. Anderson,[4] Masao Tanaka,[2] Takehisa Matsuda[1]
[1]*Department of Biomedical Engineering, Faculty of Medical Sciences, Kyushu University, Maidashi, Fukuoka 812-8582, Japan*
[2]*Department of Surgery and Oncology, Faculty of Medical Sciences, Kyushu University, Maidashi, Fukuoka 812-8582, Japan*
[3]*Department of Bacteriology, Faculty of Medical Sciences, Kyushu University, Maidashi, Fukuoka 812-8582, Japan*
[4]*Department of Pathology, Case Western Reserve University, 2085, Adelbert Road, Cleveland, Ohio 44106-4907*

Received 5 March 2004; revised 17 March 2004; accepted 19 March 2004
Published online 4 June 2004 in Wiley InterScience (www.interscience.wiley.com). DOI: 10.1002/jbm.a.30077

Abstract: We developed a novel method of evaluating biofilm architecture on a synthetic material using green fluorescent protein-expressing *Escherichia coli* and red fluorescence staining of exopolysaccharides. Confocal laser scanning microscopy observation revealed the time course of the change in the *in situ* three-dimensional structural features of biofilm on a polyurethane film without structural destruction: initially adhered cells are grown to form cellular aggregates and secrete exopolysaccharides. These cells were spottily distributed on the surface at an early incubation time but fused to form a vertically grown biofilm with incubation time. Fluorescence intensity, which is a measure of the number of cells, determined using a fluorometer and biofilm thickness determined from confocal laser scanning microscopy vertical images were found to be effective for quantification of time-dependent growth of biofilms. The curli (surface-located fibers specifically binding to fibronectin and laminin)–producing *Escherichia coli* strain, YMel, significantly proliferated on fibronectin-coated polyurethane, whereas the curli-deficient isogenic mutant, YMel-1, did not. The understanding of biofilm architecture in molecular and morphological events and new fluorescence microscopic techniques may help in the logical surface design of biomaterials with a high antibacterial potential. © 2004 Wiley Periodicals, Inc. J Biomed Mater Res 70A: 274–282, 2004

Key words: biofilm; green fluorescent protein; confocal laser scanning microscopy; *Escherichia coli*; curli

INTRODUCTION

The biomass of bacteria and extracellular materials including exopolysaccharides (EPS) that accumulate on synthetic substrates is called a biofilm.[1,2] Once a biofilm is formed on artificial implants in the body, serious, often life-threatening events or situations such as "septic shock," defined as a systemic response to infection, occur, which cannot be managed by antimicrobial drug administration due to a high level of resistance to drug diffusion into the well-stabilized biofilm bioarchitecture.[3] Implanted artificial prostheses, which are often associated with biomaterial-based biofilms, include cardiovascular implants, orthopedic replacements, intraocular implants, and intravascular catheters. Biliary stents and urinary catheters are often occluded by biofilms of *Escherichia coli*, resulting in complications in patients.[4] For cardiovascular implants, a second surgery to replace a bacterial-infected implant with a new one is often necessary.

The microbial colonization, and the nature and architecture of biofilms on synthetic polymers have been studied over a few decades. Previous studies have revealed various aspects of biofilms qualitatively as well as quantitatively, particularly focusing on adhered and proliferated cells by microscopy, plate counting, or dye-staining technique.[5–8] Electron microscopy has been used to observe the three-dimen-

Correspondence to: T. Matsuda; e-mail: matsuda@med.kyushu-u.ac.jp
Contract grant sponsor: Ministry of Health, Labour and Welfare (MHLW) of Japan, Grant-in-Aid for Scientific Research
Contract grant sponsor: Ministry of Education, Culture, Sports, Science, and Technology (MEXT) of Japan, Grant-in-Aid for Scientific Research and for the Creation of Innovations through Business-Academic-Public Sector Cooperation
Contract grant sponsor: NIH/NIBIB; contract grant number: EB-00279

sional (3D) structural features of biofilms.[9] However, this method often destroys biofilms because of complicated fixation procedures such as dehydration and fails to show an "as-is" structure.[10] Therefore, the formation of an as-is 3D structure of a biofilm of *E. coli* on synthetic polymers has not yet been fully understood.

Confocal laser scanning microscopy (CLSM) enables the high-resolution fluorescence imaging and deep optical sectioning of biological structures with negligible background interface. Additionally, CLSM enables a biofilm to be observed under hydrated conditions, thus maintaining an as-is structure without structure destruction.[11] When combined with fluorescent probes, CLSM can be effectively used for the visualization of biofilm components. In recent years, green fluorescent protein (GFP) from jellyfish *Aequorea victoria* has emerged as an *in situ* marker of living cells. EPS, which are produced by *E. coli* and which serve as structural anchors for bacterial cells in biofilms, can be specifically stained with a fluorescent dye, rhodamine-labeled lectin.[12,13] The co-use of GFP-expressing *E. coli* and rhodamine-labeled lectin under CLSM enables us to obtain in-depth information on the distribution state of the bacterial and EPS components of 3D biofilms.

The objective of this study was to perform an *in situ* visualization of the 3D structure of *E. coli*–based biofilm on polyurethane (PU) films. *In situ* monitoring using the CLSM technique enabled us to analyze the time-dependent construction of 3D-structured biofilms on a synthetic polymer. Two *E. coli* strains, curli-producing (YMel) and curli-deficient (YMel-1), were used.[14,15] Curli are surface organelles of *E. coli*, which are composed of thin fibers with a diameter of approximately 2 nm that mediate binding to adhesive proteins specific to fibronectin and laminin found in the eucaryotic extracellular matrix.[16] The significant role of curli in biofilm formation on a fibronectin-precoated substrate was clearly demonstrated.

MATERIALS AND METHODS

Bacterial strains and plasmid

The *E. coli* strains used in this study were the curli-producing strain YMel and the curli-deficient isogenic mutant strain YMel-1, both of which were transformed by electroporation with the *gfp*mut3* gene encoding plasmid DNA (pJBA27) and expressing a stable green fluorescent protein (Gfpmut3*) as previously reported.[17] *E. coli* from the frozen bacterial solution was cultured in 3 mL of modified Luria-Bertani medium containing 50 μg/mL ampicillin and 3 g/L NaCl at 37°C for 18 h under aerobic conditions, and then scaled up to a concentration of approximately 2×10^8 colony forming units per milliliter (CFU/mL), which was determined by the plate count method. Then they were diluted to a concentration of 2×10^5 CFU/mL, which was used as an initial concentration for experiments.

CLSM

The biofilms were examined by CLSM (Radiance 2000; BioRad, Hercules, CA). Square PU sheets (obtained from Olympus Optical Co., Ltd., Tokyo, Japan), which were cut to fit a six-well cell culture cluster, were sterilized using ethylene oxide, placed in a six-well cell culture cluster using sterilized forceps, and incubated with *E. coli* cell suspension (2×10^5 CFU/mL) under static condition. After 3-, 6-, 12-, and 24-h incubations, culture medium was removed and phosphate-buffered saline (PBS) was gently added to prevent drying of the biofilms. To visualize the EPS of the biofilms, rhodamine-labeled concanavalin A (5 μg/mL; Vector Laboratories, Burlingame, CA), which specifically binds to D-(+)-glucose and D-(+)-mannose groups on EPS, was used. One hundred microliters of this fluorescent solution was carefully applied on top of the biofilms grown on the PU sheet. After a 30-min incubation in the dark at room temperature, the excess staining solution was removed by four rinses with PBS. Images were recorded at an excitation wavelength of 488 nm and an emission wavelength of 515 ± 30 nm for GFP and at an excitation wavelength of 514 nm and an emission wavelength of 600 ± 50 nm for rhodamine-labeled concanavalin A.

Electron microscopy

For negative staining, *E. coli* cells, harvested from the biofilm formed on the PU sheet after a 24-h incubation, were mixed with distilled water, and the suspension was allowed to sediment for 2 min on a grid. After washing with distilled water, the specimen was negatively stained with 2% uranyl formiate and air dried before transmission electron microscopy (H-7000E; Hitachi, Tokyo, Japan).

For scanning electron microscopy (SEM), the biofilm grown on a glass slide (Matsunami Glass Industries Ltd., Osaka, Japan) after a 24-hr incubation was fixed in 2% glutaraldehyde (Electron Microscopy Sciences, Hatfield, PA) in 0.1*M* phosphate buffer for 1 h at room temperature. The fixed samples were dehydrated for 20 min at each step in an ascending acetone series, sputter-coated with platinum, and evaluated by SEM (JSM-840A; JEOL, Tokyo, Japan).

Bacterial adhesion study

The adhesion of bacteria was studied under static condition. Round PU sample sheets sterilized by ethylene oxide were placed in a 24-well cell culture cluster using sterilized forceps and incubated with *E. coli*. After 3-, 6-, 12-, and 24-h incubations, the round PU sheets were rinsed with PBS,

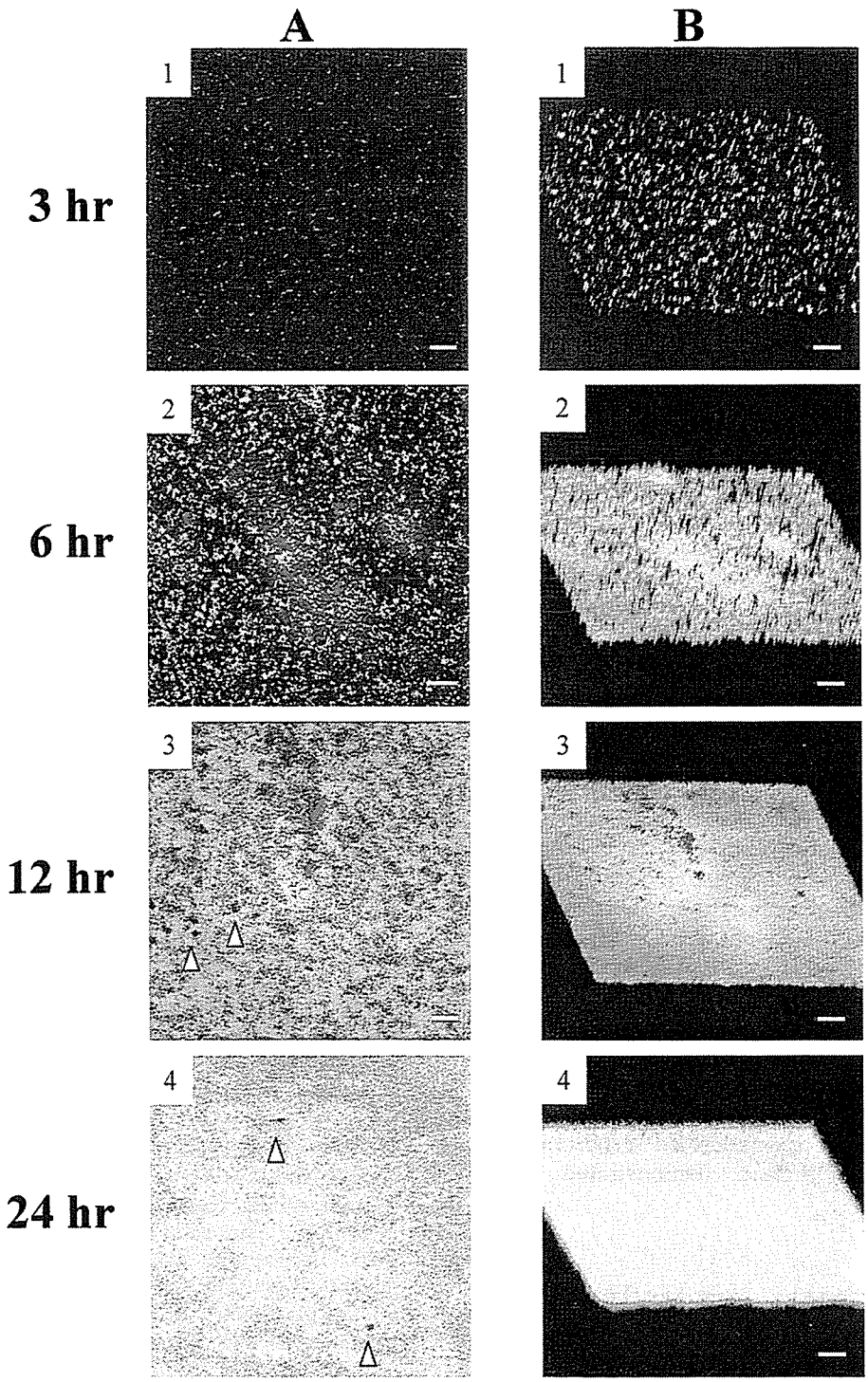

Figure 1. CLSM photographs of biofilms on PU at 3, 6, 12, and 24 h of incubations. (A) top view; (B) oblique view. Bar: 100 μm. Green and red areas indicate *E. coli* (expressing GFP) and EPS (stained with rhodamine-labeled concanavalin A), respectively. Irregular dark spots indicate water channels (white arrowheads).

placed in 15-mL Eppendorf tubes with 2 mL of PBS and sonicated for 60 s. Complete detachment of bacterial cells from the round sheets after 60-s sonication was confirmed by CLSM. Then, 100 μL of the solution containing detached bacterial cells was placed in a 96-well cell culture cluster and fluorescence intensity was measured with Molecular Imager FX (BioRad). Viable bacterial cells (CFU/cm^2) were also counted by the plate count method. Experiments were run with five samples, and the mean and standard deviation were recorded.

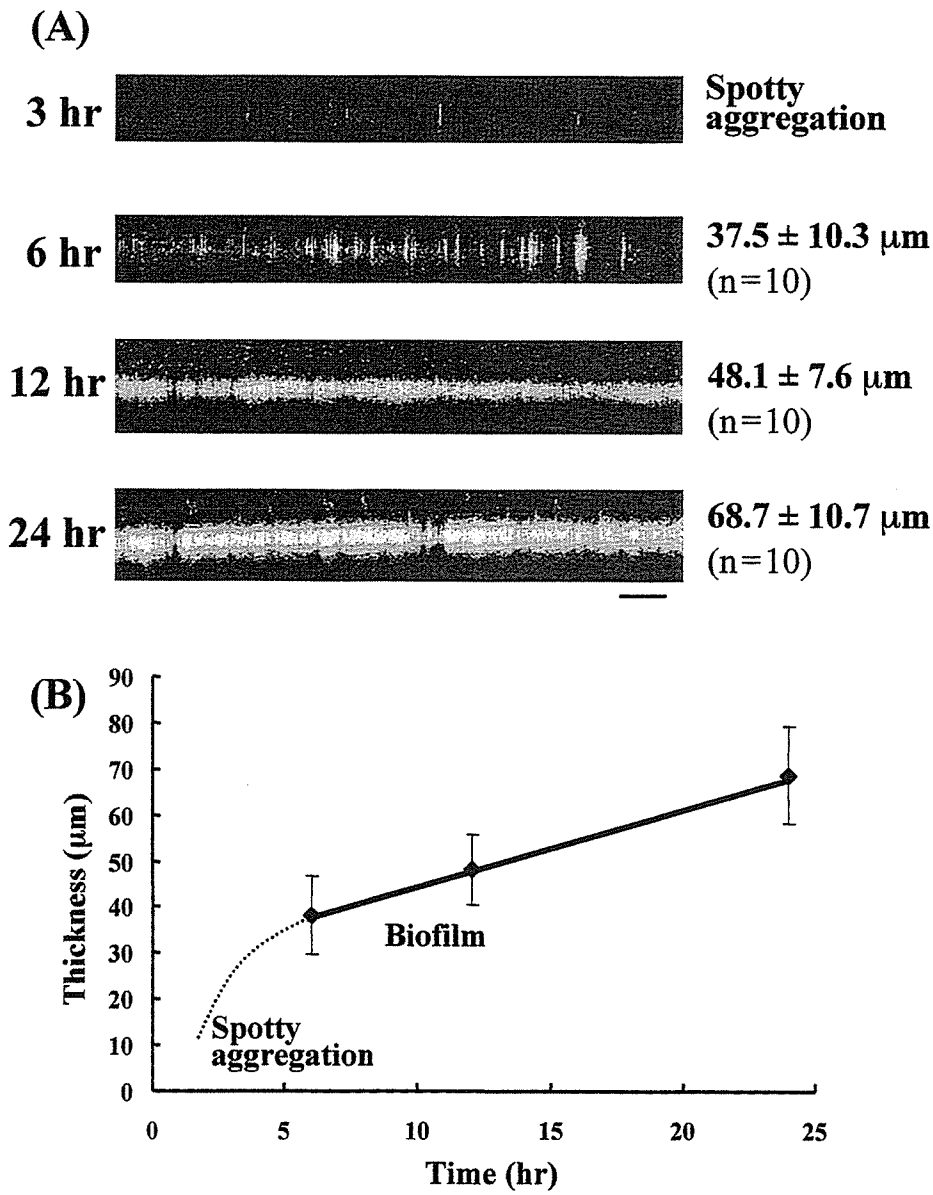

Figure 2. (A) CLSM photographs of vertical section of biofilms on PU at 3, 6, 12, and 24 h of incubations. Bar: 100 μm. (B) Biofilm thickness was determined by measuring the present images at 3, 6, 12, and 24 h of incubations. Ten vertical lines were randomly chosen for the analysis of each image. Values are expressed as means ± SD.

Protein coating of materials

Round PU sheets were incubated with bovine fibronectin (Itoham Foods Inc., Hyogo, Japan), bovine vitronectin (Yagai Co., Yamagata, Japan), and bovine serum albumin (Itoham Foods) at 1 mg/mL (0.1%) at 37°C for 24 h. Then, Luria-Bertani medium containing *E. coli* (2×10^5 CFU/mL) was poured over the protein-precoated round PU sheets and adherence was examined.

Statistical analysis

Statistical analysis was performed with the StatView 5.0 program (Abacus, Berkeley, CA). Data are shown as means ± SD. Statistical analysis was performed by analysis of variance. Differences at $p < 0.05$ were considered significant.

RESULTS

CLSM observation

To observe the 3D structure of the biofilm formed on the PU film, GFP-expressing YMel was cultured on the substrate under static condition for up to 24 h. After gentle washing with PBS, EPS generated during

biofilm formation was stained with rhodamine-labeled concanavalin A. The biofilm was observed using CLSM with time. Figure 1 shows (A) top-view and (B) oblique-view images of biofilms. At 3 h of incubation, adhered YMel cells (green color) randomly distributed without aggregate formation, and the EPS (red) formed regionally exhibited a thin cloudlike structure. At 6 h of incubation, the number of adhered YMel cells increased to form heterogeneous mosaic colonies composed of small aggregates that are scattered all over the substrate, and high-intensity red EPS regions tended to enlarge to cover the majority of the surface, thus initiating the formation of 3D structural constructs. The coexisting regions composed of green cells and red EPS were observed as a yellow region [Fig. 1(2B)]. At 12 h of incubation, the surface was completely covered with green (a major continuous matrix phase), yellow, and some spotty red regions (a dispersed domain). A small number of irregular dark spots were observed, which are supposed to be water channels, as described in the Discussion section. At 24 h of incubation, almost the entire surface area was yellowish-green, and the oblique-view CLSM image suggests that a thick biofilm was formed.

Figure 2(A) shows the time-lapse images of the vertical sections of biofilms. At the initial phase, spotty aggregates and single cells, which scattered horizontally but elongated vertically, were observed. At 6 h of incubation, the number of aggregates increased horizontally and formed a filmlike structure which enabled thickness measurement. At 12 h of incubation, the biofilm appeared more tightly packed. At 24 h of incubation, the vertical cross-sectional image revealed that EPS (yellow area) are predominantly located in the midlayer of the biofilm. To examine change in thickness with time, 10 vertical lines were randomly chosen for the measurement on each image for 6-, 12-, and 24-h incubations. Figure 2(B) shows that the average thickness of biofilms gradually increased with incubation time within the experimentally observed period.

Electron microscopic observation

The biofilm grown on glass for 24 h was observed using SEM. Figure 3 shows that *E. coli* and EPS, the matrix of the biofilm, formed a complex 3D structure. Irregularly shaped spaces resembling water channels were observed among dense structures. To confirm the expression of curli, which specifically bind to fibronectin and laminin, on the surface of *E. coli* YMel in the biofilm, negative staining was performed. Figure 4 shows a fine structure composed of thin fibers that suggest curli expression in YMel, but such a structure was not found in the curli-deficient mutant YMel-1.

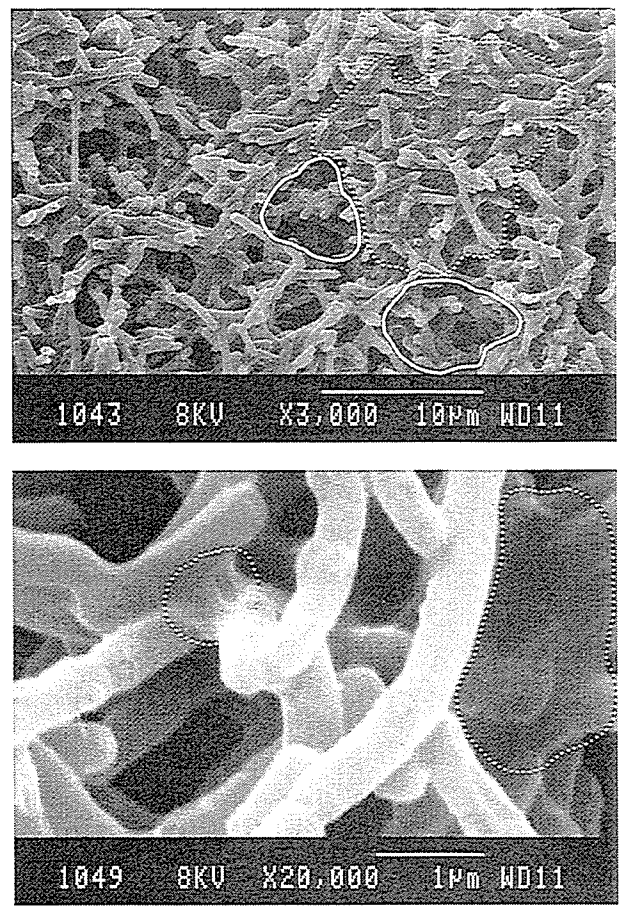

Figure 3. SEM photographs of biofilm on a glass slide at 24 h of incubation. Solid and broken lines indicate water channel regions and the dense parts of the biofilm, respectively.

Quantitative analysis

To quantify YMel cells that adhered to the PU film, round PU sheets that were incubated with YMel cells for up to 24 h postplating under static condition were subjected to gentle washing with PBS to remove nonadhering YMel cells, and then sonicated in PBS to detach all the adhered YMel cells. The fluorescence intensity of PBS containing detached YMel cells was measured with a fluorometer. In principle, the fluorescence intensity derived from GFP should correlate with the number of detached viable YMel cells by the plate count method. In fact, as shown in Figure 5, the fluorescence intensity highly correlated with the number of viable cells (correlation factor: 0.9997). The effect of the initial concentrations of YMel cells (2×10^3, 2×10^4, and 2×10^5 CFU/mL) on proliferation was studied (Fig. 6). The fluorescence intensity of PBS containing detached YMel cells increased as the initial cell concentration increased for up to 12 h of incubation. The higher the initial cell concentration, the higher the growth rate. However, after 12-h incubation, the flu-

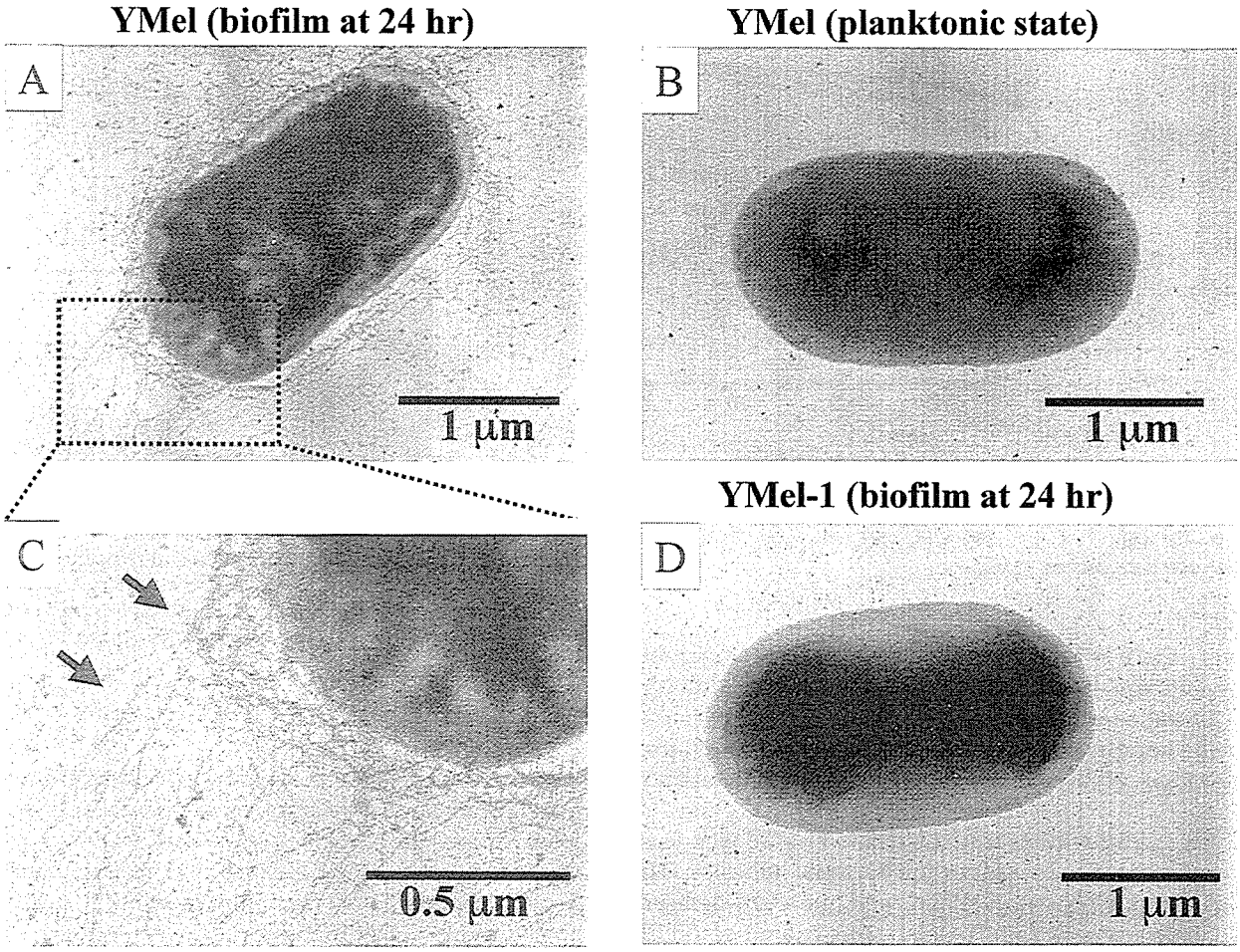

Figure 4. Transmission electron microscopic photographs by negative staining. (A) YMel in biofilm at 24 h; (B) YMel in planktonic state; (C) YMel in biofilm at 24 h with high magnification; and (D) YMel-1 in biofilm at 24 h. Arrows demonstrate curli.

orescence intensity remained almost constant, irrespective of the initial cell concentration.

Precoated-protein-dependent bacterial adhesion

To evaluate the effect of precoated proteins on bacterial adhesion, YMel was examined on round PU sheets precoated with the following proteins: fibronectin, vitronectin, and albumin (note that fibronectin and vitronectin are cell-adhesive, and albumin is non–cell-adhesive). As shown in Figure 7, for up to 12 h of incubation, there was a small significant difference in the number of adherent cells, irrespective of the type of precoated protein. However, at 24 h of incubation, the difference in the number of adherent cells was noted. The highest cell proliferation was observed on the fibronectin-coated surface, followed by the vitronectin-coated one, the proliferation potential of which was slightly higher than the noncoated surface; how-

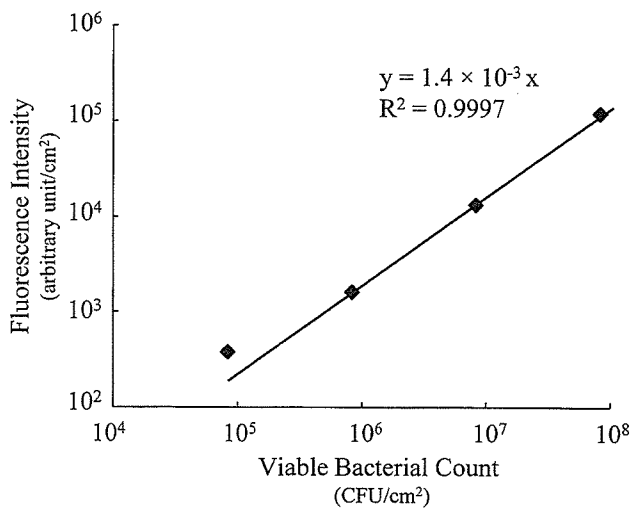

Figure 5. Correlation between fluorescence intensity and viable bacterial count in bacterial adhesion study at 24 h of incubation. The solution containing *E. coli* detached from PU sheets was diluted to different concentrations. Values are expressed as means ± SD.

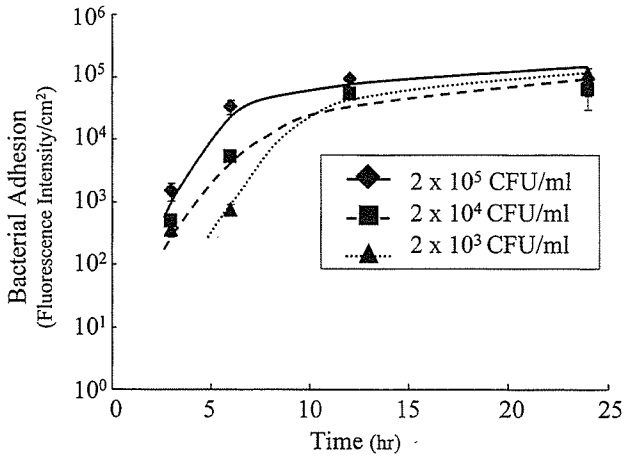

Figure 6. Time-dependent adhesion and proliferation of *E. coli* on PU. Initial concentration of bacterial cells: 2×10^3 (▲), 2×10^4 (■), 2×10^5, (◆) CFU/mL (n = 5). Values are expressed as means ± SD.

ever, there is only a small statistical difference between them. For the albumin-coated surface, although its initial adhesion potential is almost the same as that of the adhesive-protein-coated surfaces, minimal proliferation occured even with prolonged incubation time.

The curli-deficient mutant strain YMel-1 was used to determine the role of curli in bacterial adhesion. The curli-producing strain, YMel, and the curli-deficient isogenic mutant strain, YMel-1, were examined on PU surfaces with or without fibronectin coating. The number of adherent cells, measured by the plate count method, shows that the adhesion of YMel-1 was less than that of YMel to both fibronectin-coated and noncoated substrates. Precoating the PU sheets with fibronectin did not increase the adhesion of YMel-1 (Fig. 8), indicating that curli participate in fibronectin-mediated bacterial adhesion.

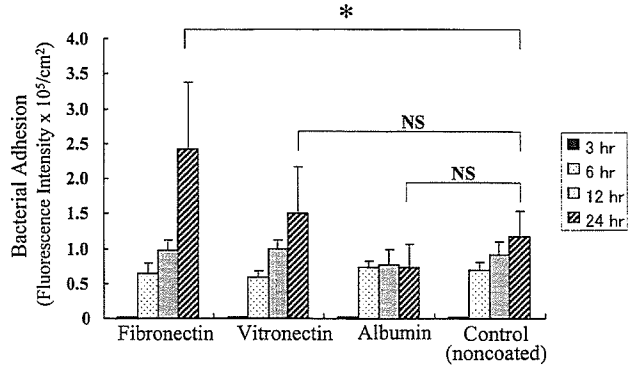

Figure 7. Bacterial adhesion to and proliferation on PU precoated with proteins at 3, 6, 12, and 24 h of incubations (n = 5). Control is noncoated PU. Values are expressed as means ± SD.

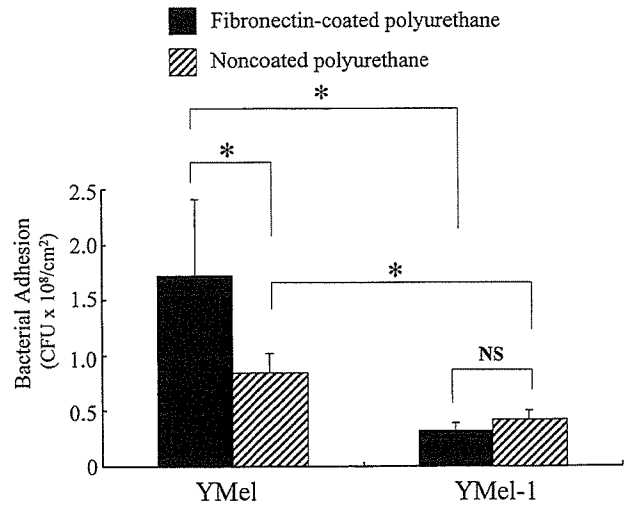

Figure 8. Bacterial adhesion and proliferation of curli-producing strain, YMel, and curli-deficient isogenic mutant strain, YMel-1 in fibronectin-coated PU and noncoated PU at 24 h of incubation (n = 5). Adhesion was determined by the plate count method. Values are expressed as means ± SD.

DISCUSSION

Bacterial adhesion is an important initial step in infection at the site of implanted biomaterials, which often causes life-threatening events in clinical situations.[1,2] Among bacteria capable of foreign-body-induced infection, *E. coli* is an important pathogen in the blockade of biliary stents or urinary catheters. The understanding of biofilm formation on synthetic biomaterials and the quantitative detection method for biofilm are key issues leading to the surface design of biomaterials with a high antibacterial adhesion potential. Electron microscopy has been used to examine biofilms on various materials.[9] However, sample preparation for electron microscopic observation requires sample dehydration, during which biofilms are often easily collapsed, structurally damaged, or destroyed. These dehydrated samples provide a deceivingly simplistic view of biofilms.[10]

To overcome this problem, we utilized fluorescent-compound-labeled *E. coli* strains that were transformed with a plasmid harboring the gene encoding GFP from jellyfish *Aequorea victoria* as an *in situ* cell marker. EPS are mainly responsible for the morphology and function of biofilms, and are considered to be key components that determine the physicochemical and biological properties of biofilms.[10,18] The co-use of GFP for bacteria and a fluorescent-compound-labeled marker specific to EPS in CLSM study provides new insights into the structure and nature of biofilm formation.

In our study, the imaging of 3D fine structures was acquired using fully hydrated samples for CLSM without any complex fixation such as the dehydration

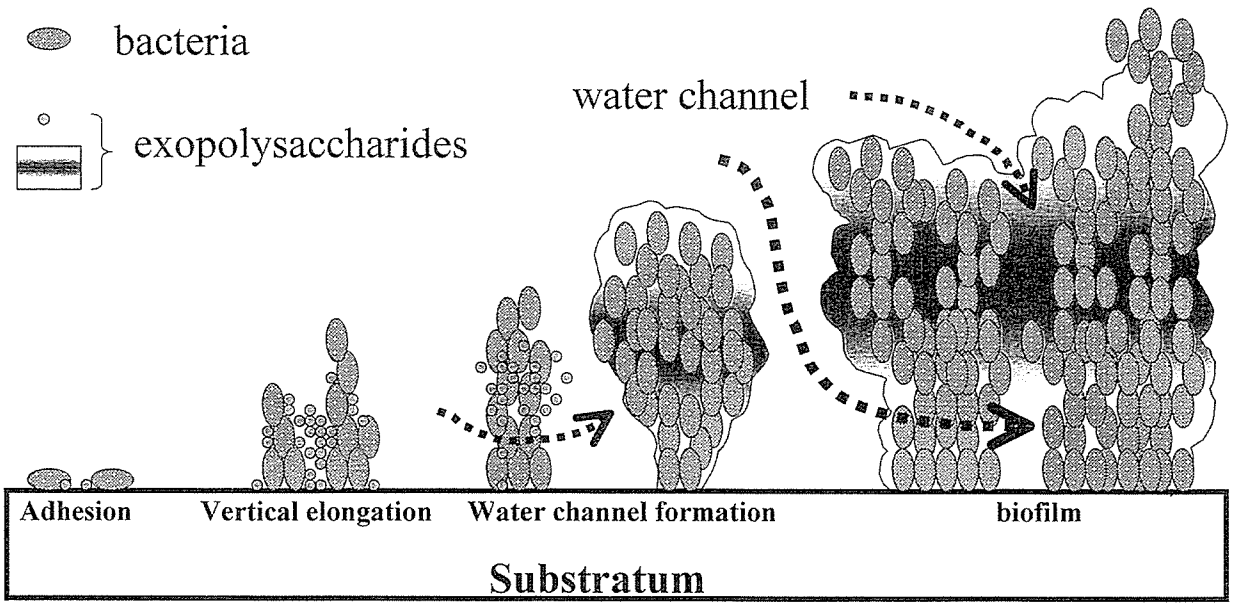

Figure 9. Scheme of time-dependent formation of biofilm architecture.

necessary in electron microscopy. In the early phase [3 h after plating: Figs. 1 and 2(A)], *E. coli* YMel emitting green fluorescence spottily aggregated on the PU surface and then vertically elongated. The number of aggregates increased with incubation time and scattered EPS-rich domains were observed [Figs. 1 and 2(A)]. Finally, a 3D structure including water channels was formed. The thickness of the biofilm increased with time, reaching to several tens of microns at 24 h after plating [Fig. 2(B)]. The channels as integral parts of the biofilm structure, which were identified as a black spotty area at 12 and 24 h of incubations (Fig. 1), are, in essence, the lifeline of the system, because they provide a means of circulating nutrients as well as exchanging metabolic products such as oxygen.[10] Interestingly, a dense interpenetrable structure of biofilm composed of *E. coli* and EPS, which was observed as the yellow region in Figures 1 and 2, existed at the middle part of the thick biofilm. Such time-dependent morphological events including bacterial adhesion, the secretion and organization of EPS, colony formation, and biofilm formation with water channels are shown in Figure 9.

As for the quantification of *E. coli* cells in biofilms, the fluorescence intensity of GFP expressed by adhered *E. coli* cells, which is directly proportional to the viable-bacterial count obtained by the plate count method (Fig. 5), allows us to easily and rapidly determine the number of adhered *E. coli* cells as compared with the conventional plate count method which requires overnight culture to detect colony formation. The growth rate of the *E. coli* cells examined for up to 24 h showed that the number of adhered and proliferated *E. coli* cells increased exponentially with time up to 12 h, and then appeared to increase at a markedly reduced rate with prolonged time, regardless of the initial bacterial cell concentration.

Many studies have reported that bacterial adhesion to and biofilm formation on material surfaces are affected by the type of protein adsorbed to the surfaces.[19–22] In the present study, three kinds of protein were preadsorbed: fibronectin and vitronectin as cell-adhesive proteins, and albumin as a non–cell-adhesive protein. Regardless of the presence or absence and the type of preadsorbed protein, there was only a small difference in the number of bacterial adhesion up to 12 h. Among the proteins tested, only fibronectin exhibited a markedly high proliferation activity only at 24 h of incubation, whereas albumin exhibited a high inhibitory activity against bacterial proliferation at 24 h of incubation. There is a small difference in bacterial proliferation activity between the vitronectin-coated and noncoated PU surfaces. This may be because the *E. coli* YMel does not produce curli in the early phase for up to 12 h of incubation but produces abundant curli (Fig. 4) in the biofilm at 24 h of incubation, although YMel does not produce curli in the planktonic state at 37°C.[23] These results are consistent with the finding by Kikuchi et al:[24] that curli were expressed in biofilm after growth at 37°C. Because curli specifically bind to fibronectin and are associated with biofilm maturation, curli-mediated biofilm formation occurred on the fibronectin-coated PU surface with a prolonged incubation time. However, the curli-deficient isogenic mutant, YMel-1, did not enhance bacterial adhesion and proliferation on the fibronectin-coated PU surface (Fig. 8).

In conclusion, we developed a novel method of deter-

mining morphological events during biofilm formation on synthetic polymers using GFP-expressing *E. coli* under CLSM observation, without the destruction of very fragile 3D structures, which may help logical surface design with a high antibacterial potential.

The authors thank T. Kikuchi, K. Yasutake, E. Koga, and M. Sato for technical assistance, and T. Kanemaru and A. Takade for electron microscopic examination.

References

1. An YH, Friedman RJ. Concise review of mechanisms of bacterial adhesion to biomaterial surfaces. J Biomed Mater Res 1998;43:338–348.
2. Gristina AG. Biomaterial-centered infection: microbial adhesion versus tissue integration. Science 1987;237:1588–1595.
3. Davies D. Understanding biofilm resistance to antibacterial agents. Nat Rev Drug Discov 2003;2:114–122.
4. Sung JY, Leung JW, Shaffer EA, Lam K, Costerton JW. Bacterial biofilm, brown pigment stone and blockage of biliary stents. J Gastroenterol Hepatol 1993;8:28–34.
5. Bryers JD, Hendricks S. Bacterial infection of biomaterials. Ann NY Acad Sci 1997;31:127–137.
6. Higashi JM, Wang IW, Shlaes DM, Anderson JM, Marchant RE. Adhesion of *Staphylococcus epidermidis* and transposon mutant strains to hydrophobic polyethylene. J Biomed Mater Res 1998; 39:341–350.
7. Merritt K, Gaind A, Anderson JM. Detection of bacterial adherence on biomedical polymers. J Biomed Mater Res 1998;39: 415–422.
8. Speer AG, Cotton PB, Rode J, Seddon AM, Neal CR, Holton J, Costerton JW. Biliary stent blockage with bacterial biofilm. A light and electron microscopy study. Ann Intern Med 1988;108: 546–553.
9. van Berkel AM, van Marle J, van Veen H, Groen AK, Huibregtse K. A scanning electron microscopic study of biliary stent materials. Gastrointest Endosc 2000;51:19–22.
10. Davey ME, O'toole GA. Microbial biofilms: from ecology to molecular genetics. Microbiol Mol Biol Rev 2000;64:847–867.
11. Cowan SE, Gilbert E, Khlebnikov A, Keasling JD. Dual labeling with green fluorescent proteins for confocal microscopy. Appl Environ Microbiol 2000;66:413–418.
12. Decho AW, Kawaguchi T. Confocal imaging of *in situ* natural microbial communities and their extracellular polymeric secretions using Nanoplast resin. Biotechniques 1999; 27:1246–1252.
13. Strathmann M, Wingender J, Flemming HC. Application of fluorescently labelled lectins for the visualization and biochemical characterization of polysaccharides in biofilms of *Pseudomonas aeruginosa*. J Microbiol Methods 2002;50:237–248.
14. Olsen A, Wick MJ, Morgelin M, Bjorck L. Curli, fibrous surface proteins of *Escherichia coli*, interact with major histocompatibility complex class I molecules. Infect Immun 1998;66:944–949.
15. Prigent Combaret C, Prensier G, Le Thi TT, Vidal O, Lejeune P, Dorel C. Developmental pathway for biofilm formation in curli-producing *Escherichia coli* strains: role of flagella, curli and colanic acid. Environ Microbiol 2000;2:450–464.
16. Olsen A, Jonsson A, Normark S. Fibronectin binding mediated by a novel class of surface organelles on *Escherichia coli*. Nature 1989;338:652–655.
17. Andersen JB, Sternberg C, Poulsen LK, Bjorn SP, Givskov M, Molin S. New unstable variants of green fluorescent protein for studies of transient gene expression in bacteria. Appl Environ Microbiol 1998;64:2240–2246.
18. Danese PN, Pratt LA, Kolter R. Exopolysaccharide production is required for development of *Escherichia coli* K-12 biofilm architecture. J Bacteriol 2000;182:3593–3596.
19. Froman G, Switalski LM, Faris A, Wadstrom T, Hook M. Binding of *Escherichia coli* to fibronectin. A mechanism of tissue adherence. J Biol Chem 1984;259:14899–14905.
20. Yu JL, Ljungh A, Andersson R, Jakab E, Bengmark S, Wadstrom T. Promotion of *Escherichia coli* adherence to rubber slices by adsorbed fibronectin. J Med Microbiol 1994;41:133–138.
21. Yu JL, Andersson R, Wang LQ, Bengmark S, Ljungh A. Fibronectin on the surface of biliary drain materials: a role in bacterial adherence. J Surg Res 1995;59:596–600.
22. Yu JL, Andersson R, Ljungh A. Protein adsorption and bacterial adhesion to biliary stent materials. J Surg Res 1996;62:69–73.
23. Bian Z, Brauner A, Li Y, Normark S. Expression of and cytokine activation by *Escherichia coli* curli fibers in human sepsis. J Infect Dis 2000;181:602–612.
24. Kikuchi T, Mizunoe Y, Takade A, Yoshida S. Curli is required for development of biofilm architecture in *Escherichia coli* K-12 and enhance bacterial adherence to human uroepithelial cells. In preparation.

nature neuroscience

Developmental switch from GABA to glycine release in single central synaptic terminals

Junichi Nabekura[1,2,5] Shutaro Katsurabayashi[1,5], Yasuhiro Kakazu[1], Shumei Shibata[1], Atsushi Matsubara[3], Shozo Jinno[4], Yoshito Mizoguchi[1], Akira Sasaki[3] & Hitoshi Ishibashi[1]

Early in postnatal development, inhibitory inputs to rat lateral superior olive (LSO) neurons change from releasing predominantly GABA to releasing predominantly glycine into the synapse. Here we show that spontaneous miniature inhibitory postsynaptic currents (mIPSCs) also change from GABAergic to glycinergic over the first two postnatal weeks. Many 'mixed' mIPSCs, resulting from co-release of glycine and GABA from the same vesicles, are seen during this transition. Immunohistochemistry showed that a large number of terminals contained both GABA and glycine at postnatal day 8 (P8). By P14, both the content of GABA in these mixed terminals and the contribution of GABA to the mixed mIPSCs had decreased. The content of glycine in terminals increased over the same period. Our results indicate that switching from GABAergic to glycinergic inputs to the LSO may occur at the level of a single presynaptic terminal. This demonstrates a new form of developmental plasticity at the level of a single central synapse.

GABA and glycine are the major inhibitory transmitters in the mammalian central nervous system. Although they act at separate receptors, they can be co-released from single synaptic terminals projecting onto spinal motor neurons and brainstem trigeminal neurons[1,2]. Postsynaptic clusters of both glycine and $GABA_A$ receptors appear to be co-localized at the subsynaptic membrane[3,4]. Furthermore, mIPSCs recorded from spinal neurons include both GABAergic and glycinergic components, suggesting that both GABA and glycine are co-released from a single synaptic vesicle[5,6]. Hence, at spinal cord synapses, GABA and glycinergic transmission is closely related, and this could have important implications for the strength and timing of motor neuron inhibition[7].

The coordinated combination of GABAergic and glycinergic inhibitory transmission is also functionally critical in the lateral and medial superior olive auditory relay neurons (LSO and MSO neurons, respectively)[8,9]. In the normal development of the auditory system, inhibitory synaptic transmission in the LSO and MSO changes from being predominantly GABAergic to being predominantly glycinergic[8,9]. Structural reorganization of the inhibitory synapses between the medial nucleus of the trapezoidal body (MNTB) and the LSO also occur throughout development[10], and it is unclear whether this switch from GABA to glycine occurs via a selective loss of GABAergic synapses and an increase in glycinergic synapses, or whether this transmitter switch occurs at individual synapses. Developmental changes in receptor subunit expression patterns have been observed in the LSO[11], but there have been no reports of a presynaptic change in the nature of the released neurotransmitter at the level of a single synapse. In the present study, we further elucidate the mechanisms contributing to this neurotransmitter switch, particularly focusing on whether presynaptic changes occur and whether they occur at single synapses.

RESULTS

Evoked IPSCs (eIPSCs) were recorded from LSO neurons in response to electrical stimulation of the ventromedial part of the LSO slice preparation. Both CNQX (10^{-5} M) and APV (10^{-5} M) were added to the external solution to block glutamatergic responses. In LSO neurons from P2 rats, bicuculline (10^{-5} M) inhibited the eIPSC by about 70%, but only caused a mild (about 15%) inhibition in P14 rats (**Fig. 1a,b**). The bicuculline-insensitive component of the eIPSC was completely abolished, at all ages, by adding strychnine (10^{-6} M). The inhibitory effects of bicuculline on muscimol and glycine responses were stable in potency throughout development (**Fig. 1c**). Thus, inhibitory synaptic transmission to LSO neurons changed from predominantly GABAergic to predominantly glycinergic during development. The switch is evident by P7, which is somewhat earlier than observed in the gerbil LSO[8], although it is virtually completed by this time for inhibitory inputs to the rat MSO[9].

To elucidate the underlying cause of this switch from predominantly GABAergic to predominantly glycinergic inputs, we concentrated on the nature of miniature IPSCs (mIPSCs), which are considered to be single quantal events[12,13]. We mechanically dissociated LSO neurons with adherent presynaptic terminals[14] (**Fig. 2a**) and recorded mIPSCs at a V_H of –60 mV in the presence of CNQX (10^{-5} M), APV (10^{-5} M) and tetrodotoxin (TTX; 3×10^{-7} M). This preparation allows us to measure spontaneous synaptic currents under good space-clamp conditions and without complications from other neurons or glia[14]. We

[1]Department of Cellular and System Physiology, Graduate School of Medical Sciences, Kyushu University, Fukuoka 812-8582, Japan. [2]Department of Developmental Physiology, National Institute for Physiological Sciences, Okazaki 444-8585, Japan. [3]Department of Otorhinolaryngology, School of Medicine, Hirosaki University, Hirosaki 036-8562, Japan. [4]Department of Anatomy and Neurobiology, Graduate School of Medical Sciences, Kyushu University, Fukuoka 812-8582, Japan. [5]These authors contributed equally to this work. Correspondence should be addressed to J.N. (nabekura@nips.ac.jp).

Published online 21 December 2003; doi:10.1038/nn1170

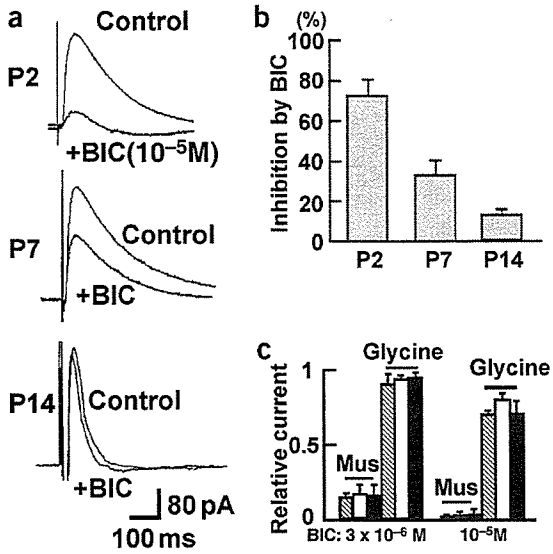

Figure 1 Developmental change in the bicuculline sensitivity of IPSCs recorded in LSO neurons in response to electrical stimulation of the ventromedial aspect of the LSO brain slice. (**a**) Five representative averaged evoked IPSCs, recorded from P2, P7 and P14 rats, in the absence (Control) and presence of 10^{-5} M bicuculline (+BIC). We used bicuculline rather than strychnine to discriminate between $GABA_A$ and glycine receptor responses because the potency of strychnine on muscimol (which affect $GABA_A$ receptors) responses varied during development (unpublished data). (**b**) Mean data showing the relative inhibition of eIPSCs by bicuculline, in LSO neurons from different developmental stages ($n = 6$, respectively). Evoked IPSCs were recorded using standard whole-cell patch-clamp techniques. V_H was 0 mV. (**c**) Inhibition of 10^{-5} M muscimol and 3×10^{-5} M glycine evoked responses by 3×10^{-6} and 10^{-5} M bicuculline, in LSO neurons from P0–2 (strip columns), P6–8 (open columns) and P14–16 (closed columns) rats. Response amplitudes are plotted relative to that observed in the absence of bicuculline ($n = 5$ or 6 in each case). The relative inhibitory effect of bicuculline on $GABA_A$ and glycine receptor mediated responses was constant throughout development.

initially pharmacologically isolated GABAergic and glycinergic components of mIPSCs in LSO neurons from P6–7 rats (Fig. 2b, left). In the presence of bicuculline (5×10^{-6} M), glycinergic mIPSCs were observed with a relatively fast decay time constant (fit from 90–10% of the mIPSC amplitude, $\tau_{gly} = 7.2 \pm 1.3$ ms, mean ± s.e.m., $n = 5$ neurons, Fig. 2c,d). In the same neurons, GABAergic mIPSCs, in the presence of strychnine (3×10^{-7} M), were observed with a much slower decay time constant ($\tau_{GABA} = 73.6 \pm 4.5$ ms, $n = 5$, Fig. 2c,d). In three other neurons, the mIPSC decay in the presence of another selective $GABA_A$ antagonist, SR-95531, was fit with a similar time constant as observed in the presence of bicuculline ($\tau_{gly} = 8.3 \pm 2.2$ ms). These results are consistent with previous reports that GABAergic mIPSCs are characterized by a longer current decay time than are glycinergic mIPSCs[6,15,16] and indicate that the mIPSCs contain both $GABA_A$ receptor– and glycine receptor–mediated components. Indeed, in control conditions, mIPSCs with two components were also detected (Fig. 2b, right). The decay of these dual-component, 'mixed' mIPSCs was fit with the sum of two exponentials, a τ_{fast} and τ_{slow}, which were 6.2 ± 0.9 ms and 58.7 ± 10.3 ms, respectively ($n = 5$; Fig. 2d). These time constants were very similar to the pharmacologically isolated τ_{gly} and τ_{GABA}, and this excellent agreement between τ_{slow} and τ_{GABA}, and between τ_{fast} and τ_{gly} was found throughout development. In neurons from P1–2 rats, τ_{fast} was 7.3 ± 3.4 ms ($n = 5$) and τ_{gly} was 8.3 ± 2.5 ms ($n = 5$), whereas τ_{slow} was 84.2 ± 8.5 ms ($n = 5$) and τ_{GABA} was 92.9 ± 10.2 ms ($n = 5$). In neurons from older rats (P16–17), τ_{fast} was 3.4 ± 1.4 ms ($n = 5$) and τ_{gly} was 3.7 ± 1.5 ms ($n = 5$), whereas τ_{slow} was 42.2 ± 6.4 ms ($n = 5$) and τ_{GABA} was 38.2 ± 7.2 ms ($n = 5$). These results show that these mixed mIPSCs reflect co-release of GABA and glycine from a single vesicle. They also show how the mIPSC decay constants get faster during development, presumably reflecting changes in receptor subunit composition[17].

Just as was observed for the eIPSCs, the chemical nature of mIPSCs also changed from predominantly GABAergic to predominantly glycinergic (Fig. 3). In the absence of any strychnine or

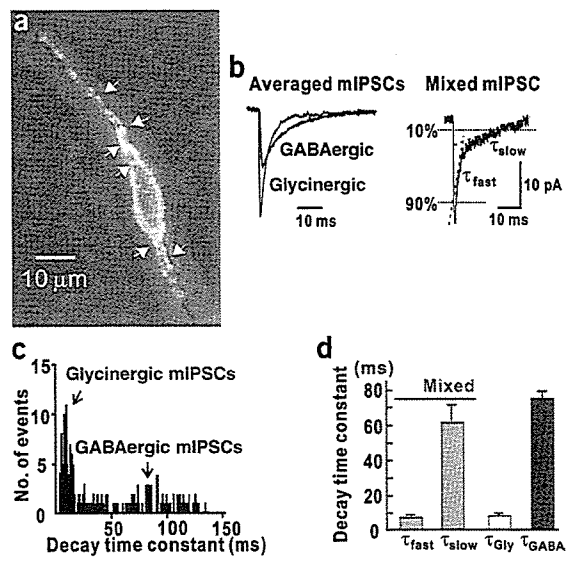

Figure 2 Pharmacological and kinetic isolation of GABAergic, glycinergic and mixed mIPSCs in voltage-clamped, isolated LSO neurons. (**a**) Photograph of a mechanically dissociated LSO neuron from P7 rats showing adherent functional synaptic boutons stained green with FM1-43. FM1-43 (1 mM) was added to the perfusate with 20 mM K^+ for 3 min, then washed out with Ca^{2+}-free, standard extracellular solution. Arrowheads indicate examples of stained synaptic boutons. (**b**) Left, averaged mIPSCs recorded in the presence of strychnine (300 nM, GABAergic mIPSC, blue, $n = 121$) and in the presence of bicuculline (5 µM, glycinergic mIPSC, red, $n = 96$) from a LSO neuron isolated from a P7 rat. Right, a 'mixed' mIPSC with a decay composed of both fast and slow components, recorded in the absence of any receptor antagonists in a LSO neuron from a P7 rat. (**c**) Distribution of the decay time constants of GABAergic (blue bars, strychnine 300 nM) and glycinergic mIPSCs (red bars, bicuculline, 5 µM) in an LSO neuron from P7 rat. Bin size, 1 ms. (**d**) Mean decay time constants for the three types of mIPSCs (mean ± s.e.m., $n = 5$ in each case). The mixed mIPSCs were fit by the sum of two exponential equations with time constants τ_{fast} and τ_{slow}, that corresponded to the decay time constants of the pharmacologically isolated glycinergic (τ_{gly}) and GABAergic (τ_{GABA}) mIPSCs, respectively.

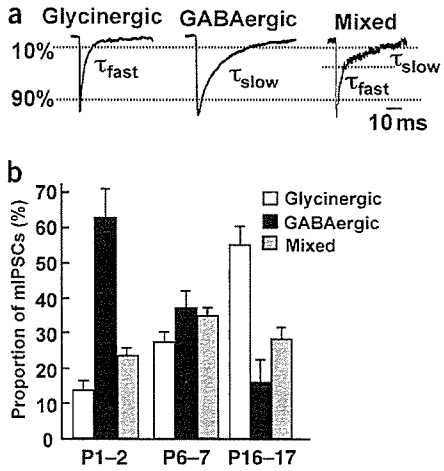

Figure 3 Developmental change in mIPSCs recorded in isolated LSO neurons. (**a**) Typical examples of GABAergic, glycinergic and mixed mIPSCs in a P6 LSO neuron. Horizontal bars indicate how the mIPSC decay, from 90% to 10% of the peak amplitude, was fit with one or two exponential functions (see **Fig. 2b**). The traces were obtained from a P6 LSO neuron. (**b**) Relative proportion of GABAergic (closed columns), glycinergic (open columns) and mixed mIPSCs (gray columns) in LSO neurons from P1–2, P6–7 and P16–17 rats. The proportion of mIPSCs of each type are expressed relative to the total number of mIPSCs recorded in each neuron (>200 events in each neuron), and are the mean ± s.e.m. of results from 10–12 neurons in each age group.

bicuculline, individual mIPSCs which were fit to either τ_{fast} or τ_{slow} were defined as glycinergic and GABAergic events, respectively (Fig. 3a). In P1–2 neurons, the proportion of total mIPSCs whose decay times indicated that they were GABAergic was 63.0 ± 7.5%, and in neurons from P16–17 the proportion was 16.0 ± 6.5%. At the same ages the proportions of glycinergic mIPSCs were 13.6 ± 2.8% and 55.3 ± 5.2%, respectively (**Fig. 3b**). The remainder of the mIPSCs had dual-component decay times (mixed mIPSCs). The incidence of these mixed mIPSCs was highest at P6–7 where they comprised 34.9 ± 2.5% of all mIPSCs ($n = 10$). In P1–2 and P16–17 rats, mixed mIPSCs comprised 23.4 ± 2.3% ($n = 10$) and 28.6 ± 3.2% ($n = 12$), respectively, of the total mIPSCs.

The mixed mIPSCs result from co-release of GABA and glycine from a single vesicle. To address whether the response to single vesicles shows a developmental change from GABAergic to glycinergic, we analyzed the relative contribution of the GABAergic (y_{GABA}) and glycinergic (y_{gly}) components to the total peak amplitude (y) of the mixed mIPSCs (**Fig. 4a**). If neurotransmitter switching also occurs at the level of single synapses, the GABAergic component in the mixed mIPSCs would be expected to decrease with age and the glycinergic component would increase. The absolute amplitude of the glycinergic component increased with age: 15.6 ± 3.2 pA at P1–2, 27.9 ± 3.6 pA at P6–7 and 43.4 ± 8.2 pA at P16–17 (n = 10–12 neurons at each age). The amplitude of the GABAergic component also increased from P1–2 (10.5 ± 2.9 pA, $n = 10$) to P6–7 (19.0 ± 1.5 pA, $n = 10$), before declining again in older rats (13.3 ± 1.7 pA at P16–17, $n = 12$, Fig. 4c). The relative contribution of the GABAergic component to the total mixed mIPSC amplitude (y_{GABA}/y) was not significantly different between P1–2 and P6–7 rats, but was decreased in older (P16–17) rats (38.9 ± 3.5% at P1–2, 53.2 ± 5.9% at P6–7 and 25.8 ± 3.9% at P16–17, **Fig. 4b,d**). Thus, the contribution of GABA to the response to a single vesicle declines in older rats, whereas that of glycine increases, consistent with neurotransmitter switching occurring at a single synapse.

The above results demonstrate a developmental switch from GABAergic to glycinergic neurotransmission at single synapses but do not distinguish whether this change occurs presynaptically (that is, a single terminal switches from GABA to glycine release), or postsynaptically (that is, a change in subsynaptic receptors from $GABA_A$ to glycine[8,11] with a constant co-release of GABA and glycine throughout development[16]), or a combination of both. The mean responses of LSO neurons to exogenous GABA and glycine were not significantly different throughout development. Specifically, GABA (3×10^{-5} M) induced an inward current at a V_H of –60 mV of 305 ± 68 pA in neurons from P0–2 rats, 409 ± 38 pA from P7 rats and 364 ± 82 pA from P14 rats ($n = 5$ or 6 neurons at each age). At the same ages the response to glycine (10^{-4} M) was 297 ± 57 pA at P0–2, 349 ± 84 pA at P7 and 305 ± 58 pA at P14 ($n = 5$ or 6). Therefore, there does not seem to be any gross developmental change in the response of the extrasynaptic receptors, although this may not reflect what is occurring at the subsynaptic receptors.

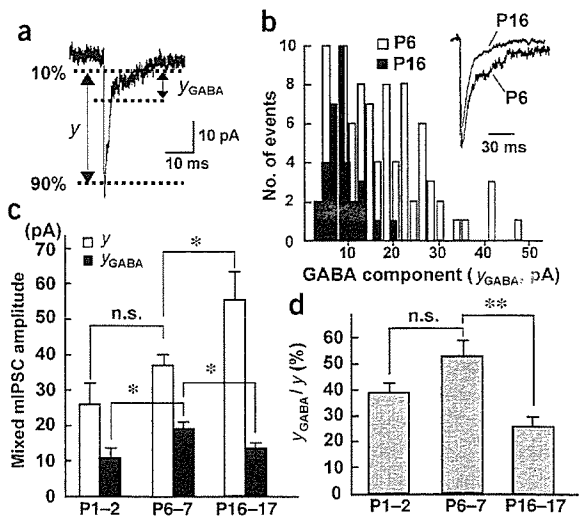

Figure 4 Developmental decrease in the contribution of the GABAergic component to mixed mIPCSs. (**a**) Example of a mixed mIPSC to illustrate the meaning of y (the peak mIPSC amplitude) and y_{GABA} (the amplitude of the mIPSC due to the GABAergic component). Individual events were fit with the double exponential function: $y = y_0 + y_{fast}\, e^{(-x/\tau fast)} + y_{slow}\, e^{(-x/\tau slow)}$, in which y_{fast} and y_{slow} were defined as $y_{glycine}$ and y_{GABA} and their sum as y. (**b**) Distribution of y_{GABA} in mixed mIPSCs from typical P6 (open bars) and P16 (black bars) LSO neurons. mIPSCs from P6 and P16 neurons were scaled so as to make their peak amplitudes equivalent. Note that the GABAergic component (y_{GABA}) of the mixed mIPSCs in P16 LSO neurons was smaller than that in P6 LSO neurons. Bin size, 2 pA. (**c**) Comparison of the mean absolute peak amplitude of mixed mIPSCs (y, open bars) and the mean amplitude of the GABAergic component (y_{GABA}, closed bars) in different age groups. Note the steady increase in y throughout development and the smaller contribution of y_{GABA} in the P16–17 rats. (**d**) Relative contribution of the GABAergic component to the peak amplitude of the mixed mIPSCs (y_{GABA}/y) at different developmental stages. Note the marked decrease in y_{GABA}/y after P6–7.

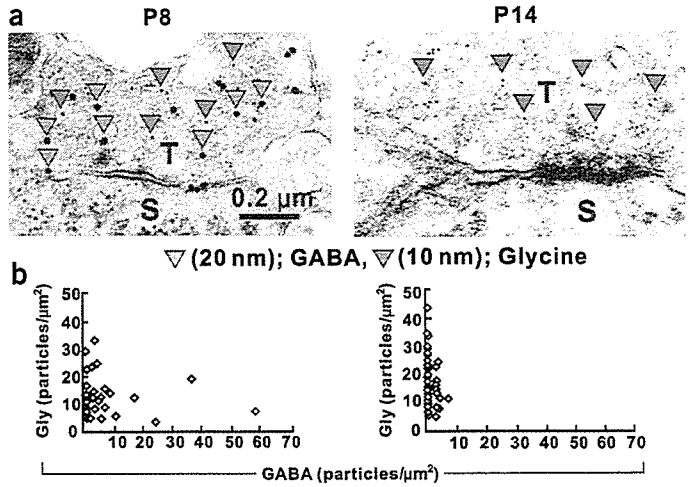

Figure 5 Quantitative analysis of GABA and glycine content in presynaptic terminals using immunogold staining and electron microscopy. (**a**) Typical electron micrographs of a synapse on to an LSO neuron; in a P8 (left) and P14 (right) rat. The large (20 nm) gold particles indicated with blue arrow heads are coated with antibodies specific to GABA, whereas the smaller (10 nm) gold particles are coated with antibodies to glycine (red arrowheads). T, presynaptic terminal; S, soma of postsynaptic cell. (**b**) Summary of group data from the immunogold experiments in P8 (left) and P14 (right) LSO neurons. Number of GABA-reactive particles/μm^2 in each inhibitory synapse is plotted against the number of glycine-reactive gold particles observed in the same synapse (total number of terminal micrographs observed were 58 from three P8 rats, and 80 from three P14 rats). Note that all inhibitory synapses observed contained glycine, but significant quantities of GABA were only colocalized in these synapses from the P8 neurons. The number of glycine particles was greater in P14 synapses than in P8 synapses ($P < 0.05$, unpaired t-test). The specificity of each antibody was examined using control experiments (**Supplementary Fig. 2**).

We also examined any presynaptic changes during development by looking directly at the composition of transmitters in single presynaptic terminals using an immunogold technique and electron microscopy (**Fig. 5**). Many terminals showed a background stain of about 1–5 gold particles/μm^2, so only terminals with a total number of GABA- and glycine-reactive particles greater than this background level were considered to be clearly inhibitory synapses and included in the subsequent analysis (**Supplementary Fig. 1** online). At P8, 38/58 terminals satisfied this criterion, and at P14, 41/80 terminals were included. At P14, the density of glycine-reactive gold particles in a single terminal was 18.6 ± 1.5/μm^2 (mean ± s.e.m., $n = 41$), which was significantly larger than observed at P8 (11.8 ± 1.2 particles/μm^2, $n = 38$, $P < 0.05$, unpaired t-test, **Fig. 5b**). In contrast, the GABA particle density in single terminals significantly decreased over the same period, from 4.9 ± 1.8/μm^2 at P8 ($n = 38$) to 0.9 ± 0.30/μm^2 at P14 ($n = 41$; $P < 0.05$). The percentage of terminals where both GABA- and glycine-reactive gold particles were observed, decreased from 50% at P8 (19/38 terminals) to 32% (13/41) at P14. Hence, switching of inhibition from GABAergic to glycinergic is also reflected in an increase in glycine content in terminals, a decrease in the proportion of terminals containing GABA, and a decrease in the extent of GABA in terminals where both transmitters are present.

One mechanism that potentially could decrease the amount of GABA in single presynaptic terminals is a decrease in the synthesis of GABA in the LSO. To investigate this possibility, we used immunohisto-chemistry and confocal microscopy to examine levels of the GABA synthesizing enzyme, glutamic acid decarboxylase (GAD). For comparison, we also stained for glycine in these experiments. The glycine antibody staining in the LSO markedly increaseed in intensity during development, whereas GAD antibody staining (which recognizes both GAD 65 and GAD 67) seemed to decrease in intensity over the same period (**Fig. 6**). At higher resolution (**Fig. 6g–l**), similar changes in the number of GAD- and glycine-reactive puncta are seen, although several terminals still showed clear GAD staining even at P18 (**Fig. 6k**). This developmental pattern of glycine staining parallels that observed in the immunogold experiments (**Fig. 5**). The decrease in GAD staining suggests that a decrease in GABA synthesis contributes to the decrease in the GABA content in individual terminals.

Finally, we examined whether the extent of occupation of the postsynaptic GABA receptor clusters changes during the transitional period when the contribution of GABA to mIPSCs is changing. In three out of seven neurons from P6 rats, diazepam (3×10^{-7} M) increased the mean amplitude of mIPSCs by about 6–16%. This suggests that, for these three neurons, the GABA content in a single vesicle does not saturate the subsynaptic $GABA_A$ receptors. Given that the concentration of GABA in the synaptic cleft at individual release sites is typically sufficient to saturate postsynaptic $GABA_A$ receptor clusters in central neurons[18], this result further supports the decreased content of GABA in single vesicles and suggests that the presynaptic decreases in GABA may occur before significant decreases in the number of postsynaptic receptors[11].

DISCUSSION

In the present study, we used both electrophysiological analysis of mIPSCs and immunohistochemistry to show that the neurotransmitter phenotype of single presynaptic inhibitory terminals changes from GABAergic to glycinergic during the first two postnatal weeks. An initial period of expansion of both MNTB terminal arborizations and LSO dendrites in the first one or two postnatal weeks is followed by a refinement of these processes and a loss of synaptic specializations[19]. Recent studies indicate that the functional elimination of inhibitory inputs from MNTB to the LSO may occur before the structural changes, even within the first two weeks[20]. If synapse elimination and refinement were solely responsible for this presynaptic switch, terminals would need to be selectively eliminated based on subtle differences in their relative presynaptic GABA and glycine content, and sequentially replaced with glycinergic terminals containing an increasing amount of glycine and a decreasing amount of GABA. We strongly favor a much simpler hypothesis; that the concentration of glycine increases, while that of GABA decreases, in single terminals. This inference is also supported by the decrease in GAD levels (**Fig. 6**). Considering that the vesicular inhibitory amino acid transporter (VIAAT) can pump both GABA and glycine into the presynaptic vesicles[21], this developmental change in terminal GABA/glycine content is then reflected in the vesicular content of GABA/glycine and the

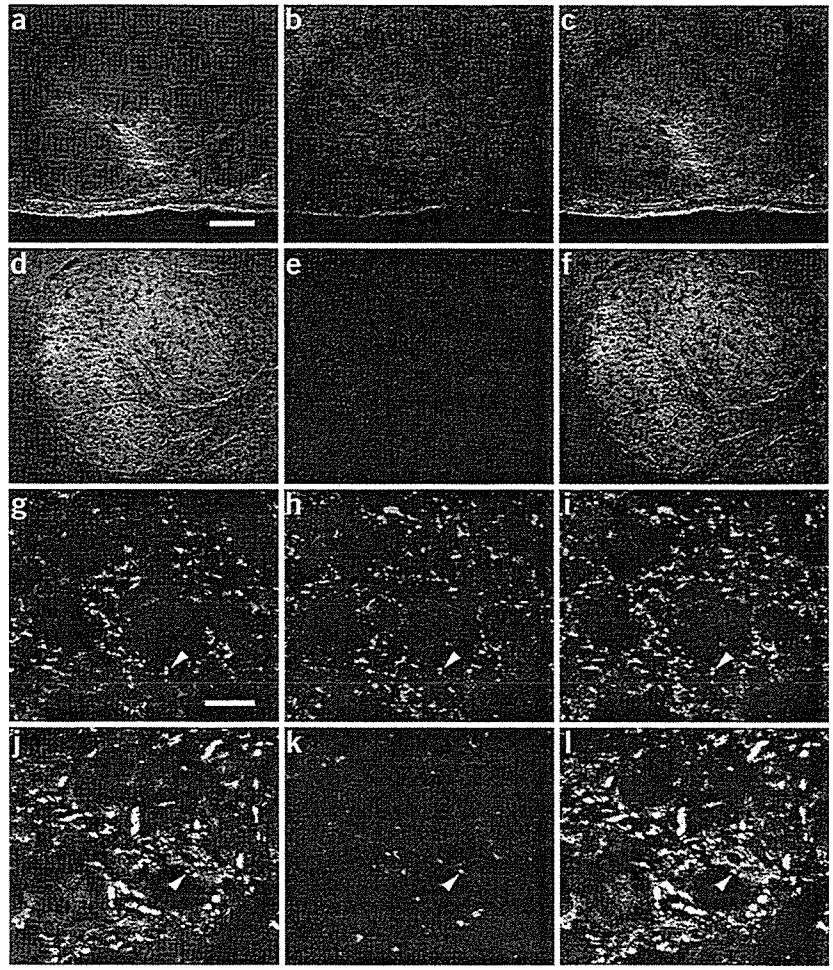

Figure 6 Immunohistochemical staining of GAD and glycine in the developing LSO. Immunofluorescent double-labeled confocal laser scanning microscope images for glycine (**a,d,g,j**), glutamic acid decarboxylase (GAD; **b,e,h,k**) and when both images are merged (**c,f,i,l**). Both lower-magnification images (**a–f**) and higher-power images (**g–l**) from sections from P5 (**a–c**, **g–i**) and P18 rats (**d–f**, **j–l**) are shown. At P5, there is weak glycine immunoreactivity throughout the LSO but intense GAD immunoreactivity (**a–c**). The high-power images (**g–i**) further show that only a few glycine-positive puncta exist in the LSO, whereas there are numerous GAD-positive puncta. At P18, the low-power images (**d–f**) show the intense glycine immunoreactivity and the weak GAD immunoreactivity in the LSO. The high-power images (**j–l**) reveal that many glycine-positive puncta are present in the LSO, but there are only a few GAD-positive puncta. Arrowheads indicate example boutons containing both glycine and GAD immunoreactivity. The scale bar in **a** applies to the low-power images (**a–f**; 100 μm); the scale bar in **g** applies to the high-power images (**g–l**; 10 μm). Under our experimental conditions, soma staining for GAD and glycine in the LSO neurons is not shown as clearly as that for the presynaptic boutons. Staining and image-capturing conditions were optimized for visualization of boutons.

decay time course of the mixed mIPSCs. Our preliminary data indicate that VIAAT is expressed at relatively high levels in the rat LSO. A change in the content of neurotransmitter, from noradrenaline to acetylcholine, has also been found in peripheral sympathetic nerve terminals following innervation of their targets in the sweat gland[22,23]. A switch from GABA to glycine has already been reported for IPSCs evoked by stimulation of multiple MNTB inputs[8–11], but here we provide new evidence that neurotransmitter switching at a central synapse can occur at the level of a single presynaptic vesicle.

One intriguing result from the present study is that although the switch from GABAergic to glycinergic eIPSCs was evident at P7 (Fig. 1) and there was a decline in the proportion of GABAergic mIPSCs over the same period, the contribution of GABA to the mixed mIPSCs did not significantly decrease until after the second postnatal week (Fig. 4). One possible explanation for this difference is that switching of terminal and vesicle neurotransmitter content may occur over a shorter time period in individual terminals, but these effects in a population of terminals may not be apparent until later. For example, pure GABAergic terminals may be converted to a mixed phenotype in the first postnatal week, while at the same time, other mixed terminals are converted to pure glycinergic terminals (and hence would no longer be included in the population of mixed mIPSCs). If such temporal heterogeneity does occur, one may not expect to see changes in the population responses until all the terminals had already showed significant switching.

Presynaptic changes in neurotransmitter content, that is, an increase in glycine and a decrease in GABA, can be added to the range of changes in inhibitory synaptic transmission and its modulation that have been reported in the LSO throughout development. Morphological changes include extensive remodeling of pre- and postsynaptic elements. In the first postnatal week, expansion of MNTB afferents is apparent in the gerbil LSO, and this is followed by a more prolonged period (for up to 4 weeks) of refinement and elimination of both the terminal boutons and the LSO dendrites[10,19]. For the rat LSO, the number of dendritic end-points begins to decline during the first postnatal week, although the most marked decreases in the relative size of LSO dendrites and their fields occurs after P14 (ref. 24). Synapse elimination and functional reorganization of MNTB–LSO connections have also been recently demonstrated in the rat[20]. In this previous study, the functional refinement of the inhibitory inputs was completed by P8, suggesting that functional refinement of the inhibitory inputs may precede structural refinements. The shift from GABAergic to glycinergic eIPSCs in the gerbil occurs slightly later than observed for rat LSO (Fig. 1) and MSO inputs[9]—it is only about 40% complete by P8 (ref. 8). If synapse elimination is in fact completed by P8 in the rat, this would further support our hypothesis of changes in transmitter content in preexisting synapses. Our demonstration of mixed mIPSCs also indicates that glycine and $GABA_A$ receptors are colocalized at LSO synapses. Changes in receptors and their associated accessory proteins have also been reported in the developing LSO. Gephyrin immunoreactivity is very low at birth in the gerbil LSO but increases markedly over the first few weeks[8]. Antibody staining for $GABA_A$ receptor subunits β2

and β3 shows a parallel decline over this period[8]. Expression of the glycine α1 receptor subunit increases markedly over the first 2 weeks[10], replacing the neonatal (presumed α2) receptor isoform. This subunit switch is likely to contribute to the briefer decay times of glycinergic mIPSCs over the course of development[25]. The increased amplitude of glycinergic mIPSCs could also reflect changes in subsynaptic receptors, although we did not observe any developmental change in the amplitude of responses to exogenous glycine.

What could be the functional significance of the switch from GABAergic to glycinergic transmission? Both GABA and glycine depolarize neonatal LSO neurons due to their high intracellular Cl^- content[26,27]. The depolarizing GABA/glycine responses in the rat LSO convert to hyperpolarizing responses during the first two postnatal weeks[26]. This occurs because, in more mature neurons, the outwardly directed Cl^- transporter, KCC-2, is integrated into the plasma membrane and becomes functional[28]. The longer-duration GABAergic responses observed in this study and others[9] would be expected to produce a more prolonged depolarization than glycine would produce, thereby allowing greater Ca^{2+} influx. In fact, Ca^{2+} transients in response to MNTB stimulation have been observed in rat and mice LSO neurons during the first postnatal week[29]. The Ca^{2+} transients generated by exogenous GABA were also larger than those generated by exogenous glycine (although the synaptic Ca^{2+} transients were similar for GABAergic and glycinergic inputs)[29]. GABA-induced membrane depolarization in immature neurons has been shown to be important for neuronal maturation[30–32]. The aggregation of glycine receptors by gephyrin, for example, is promoted by Ca^{2+} influx through channels in the postsynaptic membrane[33]. Thus, GABA-induced elevation of Ca^{2+} might be similarly important for insertion of glycine receptors into the subsynaptic membrane in developing LSO neurons.

Another possible contribution from the GABAergic inhibition in the younger rats concerns $GABA_B$ receptor–mediated responses. In LSO neurons from P4–P8 rats, postsynaptic $GABA_B$ receptors mediate a form of frequency-dependent synaptic plasticity[34,35]. Hence GABAergic neurotransmission may also be important in developing LSO neurons due to actions via $GABA_B$ receptors.

In the adult, the briefer hyperpolarizing responses mediated by glycine receptors would be more appropriate for accurate processing of temporal differences in the sound input from both ears. Our results show that, in addition to synaptic remodeling and changes in postsynaptic receptors, changes in the neurotransmitter content of presynaptic terminals and their vesicles also contribute to the developmental switch from GABAergic to glycinergic inhibition in the rat LSO.

METHODS

All experiments were performed in accordance with the Guiding Principles for the Care and Use of Animals approved by the Council of the Physiological Society of Japan.

Electrophysiology. Wistar rats, at 1–17 d after birth (P1–P17), were quickly decapitated under ether anesthesia. Coronal midbrain slices containing the LSO were made (280-350 μm thickness) as previously described[36]. The ionic composition of the internal (patch pipette) solution for the whole-cell recordings contained 50 mM CsCl, 30 mM Cs_2SO_4, 0.5 mM $CaCl_2$, 2 mM $MgCl_2$, 5 mM EGTA, 5 mM TEA-Cl, 5 mM Mg-ATP and 10 mM HEPES. pH was adjusted to 7.2 with Tris-base. QX-314 (5 mM, Research Biochemicals) was added to the internal solution to block voltage-dependent Na^+ channels. The external solution for the brain slice recordings contained 124 mM NaCl, 5 mM KCl, 1.2 mM KH_2PO_4, 1.3 mM $MgSO_4$, 2.4 mM $CaCl_2$, 10 mM glucose, 24 mM $NaHCO_3$, and was well-oxygenated with 95% O_2/5% CO_2.

Single LSO neurons were mechanically dissociated from brain slices, so as to preserve functional presynaptic nerve terminals[15] (Fig. 2a). The internal patch-pipette solution for these recordings was as described above. The standard external solution contained 150 mM NaCl, 5 mM KCl, 1 mM $MgCl_2$, 2 mM $CaCl_2$, 10 mM HEPES and 10 mM glucose (pH 7.2). Antagonists and agonists were applied to acutely dissociated LSO neurons using a Y-tube perfusion device[37]. Neurons were pre-incubated with receptor antagonists for at least 30 s before recording data or applying agonists.

Spontaneous mIPSCs were acquired using pClamp 8.2 (Axon Instruments) and analyzed using both pClamp 8.2 and the MiniAnalysis program (Synaptosoft). Events were detected using an amplitude threshold of 2 pA and events were further rejected or accepted on the basis of their rise and decay times. Large numbers of mIPSCs (>200) were obtained from each neuron recording. mIPSC decay time constants were obtained by fitting a double exponential function to the mIPSC decay from the time period corresponding to between 90% and 10% of the peak mIPSC amplitude. Individual events were fitted (with >150 iterations) to the function: $y = y_0 + y_{fast}\, e^{(-x/\tau fast)} + y_{slow}\, e^{(-x/\tau slow)}$. mIPSCs where considered to have a mono-exponential decay when the relative contribution of one of the exponential distributions was <1%. Thus, the decision about whether a single mIPSC decayed with a single or dual components was completely objective. The proportion of GABAergic, glycinergic or mixed mIPSCs, in each recording, was automatically determined from the distribution of mIPSC decays. Numerical values are presented as means ± standard error of the mean (s.e.m.).

Post-embedding immunohistochemistry. Rats were deeply anesthetized with sodium pentobarbital (100 mg per kg body weight) and transcardially perfused with saline, followed by 15 min perfusion with fixative (a mixture of 2.5% glutaraldehyde and 4% paraformaldehyde in 0.1 M phosphate buffer). The brainstem was removed and incubated overnight (4 °C) in the same fixative. Subsequently, small blocks of brainstem, containing the LSO, were treated with 1% OsO_4, dehydrated in ethanol and propylene oxide, and embedded in Durcupan (ACM Fluka). Ultrathin slices were cut and mounted on nickel grids. Postembedding double immunogold labeling of GABA and glycine was performed as described[38]. The GABA antibody (1:8,000, gift of O.P. Ottersen, University of Oslo, Oslo, Norway) was visualized using an IgG coupled to 20 nm gold particles (GAR 20; 1:20, British Biocell International). The glycine antibody (1:1,000, Biogenesis) was visualized using a Fab fragment coupled to 10 nm gold particles (GFAR 10; 1:20, British Biocell International). The ultrathin specimens were initially incubated for GABA immunogold labeling, followed by that for glycine labeling. Specimens were exposed to formaldehyde vapor for 1 h at 80 °C to avoid any interference between the sequential incubations. Specimens only stained positive for the 20 nm gold-conjugated particles when they were incubated with the GABA-specific antibody while the smaller gold-conjugated particles were only observed when specimens contained the glycine-specific antibody (**Supplementary Fig. 2** online). The specificity of the antibodies under our conditions was tested[39]. Brain sections were processed alongside control sections containing a series of different amino acids gluteraldehyde-conjugated to brain macromolecules. For quantification of the amount of presynaptic glycine and GABA we manually counted the number of gold particles observed within presynaptic terminals that could be clearly seen to synapse onto the soma. Many terminals examined contained a low level of staining for GABA and glycine reactive gold particles (1–4 particles/μm^2). A second population contained a greater density of gold particles (**Supplementary Fig. 1** online). The presence of >5 particles/μm^2 was the only criteria used to accept inhibitory terminals for study. To compare particle density across different terminals and specimens, results are expressed as particles/μm^2. Three rats from each age group were used and the specimens derived from rats at the two different ages were grouped together. Sections contained terminals that synapsed on to the soma, or on the larger proximal dendrites.

Immunocytochemistry. Rats were deeply anesthetized with sodium pentobarbital (100 mg/kg body weight), and then were transcardially perfused with phosphate buffered saline (PBS, pH 7.4) followed by a mixture of 2% paraformaldehyde and 2.5% glutaraldehyde in 0.1 M phosphate buffer (pH 7.4). The brains were left *in situ* for 1–2 h at room temperature (22–24 °C) and then were removed from the skull. Small blocks containing the LSO were separated from the brain and then sliced transversely into 50 μm-thick serial sections. The thin sections were incubated in 30% sucrose in 0.1 M phosphate buffer (pH 7.4) for 1 h, and were then freeze-thawed in liquid nitrogen.